TECHNICAL REVIEWS

Guide to optical spectroscopy of layered semiconductors

Shivangi Shree, Ioannis Paradisanos, Xavier Marie, Cedric Robert and Bernhard Urbaszek

Abstract | Potential applications in photonics and optoelectronics are based on our understanding of the light–matter interaction on an atomic monolayer scale. Atomically thin 2D transition metal dichalcogenides, such as MoS_2 and WSe_2, are model systems for layered semiconductors with a bandgap in the visible region of the optical spectrum. They can be assembled to form heterostructures and combine the unique properties of the constituent monolayers. In this Technical Review, we provide an introduction to optical spectroscopy for layered materials as a powerful, non-invasive tool to access details of the electronic band structure and crystal quality. We discuss the physical origin of the main absorption and emission features in the optical spectra and how they can be tuned. We explain key aspects of practical set-ups for performing experiments in different conditions and the important influence of the direct sample environment, such as substrates and encapsulation layers, on the emission and absorption mechanisms. A survey of optical techniques that probe the coupling between layers and analyse carrier polarization dynamics for spin- and valleytronics is provided.

The physical properties of atomic monolayers are often very different from those of their parent bulk materials. Prime examples are graphene and monolayers of MoS_2, as their ultimate thinness makes them extremely promising for applications in electronics and optics. At the same time, they give access to new degrees of freedom of the electronic system (such as the valley index) or interactions between quasiparticles such as excitons (Coulomb-bound electron–hole pairs). Additional functionalities emerge as these materials are stacked in van der Waals heterostructures[1]. In addition to the materials currently being investigated, about 1,800 materials are now predicted to be exfoliable and stable in monolayer form[2]. Tools for investigating the properties of these emerging layered materials are therefore of prime importance. In this Technical Review, we provide a guide to optical emission and absorption spectroscopy for atomically thin layered materials, commonly carried out in optical microscopes for increased spatial resolution. Optical spectroscopy gives access to key information such as the bandgap, exciton binding energy and absorption strength of a material. Combining spatial and polarization resolution gives access to the spin and valley physics in monolayers and also in heterostructures. In the latter, optical transitions are tunable over a wide wavelength range, and electron–hole pairs can experience nanoscale moiré confinement potentials, which can be used for quantum optics experiments and for investigating collective effects of electronic excitations[3,4]. Moreover, optical spectroscopy techniques can be applied to semiconducting, magnetic layered materials such as chromium trihalides to probe their magnetization[5–7]. Optical spectroscopy also reveals magnetic proximity effects and charge transfer as non-magnetic and magnetic layers are placed in direct contact to form heterostructures[8–10]. For applications in photonics, such techniques reveal how light–matter coupling is enhanced when layered materials are placed in optical cavities or on resonators[11,12]. Optical spectroscopy can be used as a non-invasive technique for studying lattice structure, interlayer coupling and stacking that complements direct atomic-resolution imaging from electron microscopy[13–17].

This Technical Review aims to give an overview of the kind of information on layered materials that we can access in practical optical spectroscopy: how the optical spectra are affected by several distinct parameters such as the set-up and equipment used, the experimental conditions (temperature and external fields), the sample structure and, very importantly, the direct environment of the active layer. Electronic excitations in an atomically thin layer are strongly affected by the substrate and encapsulating layers. This leads to two directions for experiments. First, it enables access to intrinsic properties of the layers in a well-controlled environment (between two inert buffer layers). Second, the layered

Université de Toulouse, INSA-CNRS-UPS, LPCNO, Toulouse, France.

✉*e-mail: shree@insa-toulouse.fr; paradeis@insa-toulouse.fr; urbaszek@insa-toulouse.fr*

https://doi.org/10.1038/s42254-020-00259-1

Key points

- Optical spectroscopy tools give access to details of the electronic band structure, crystal quality, crystal orientation, light–matter interaction and spin–valley polarization of 2D materials.
- Key experimental parameters such as temperature, applied electric and magnetic fields, optical excitation power and the direct sample environment (such as substrate and encapsulation layers) strongly influence optical absorption and emission.
- To achieve high spatial resolution, experiments on layered materials are carried out in optical microscopes. The high numerical aperture of the microscope objectives results in excitation and collection of light away from normal incidence, which gives access to information on optical transitions with different spatial orientations of the optical dipole.
- In layered materials with strong excitonic effects, light–matter interaction is enhanced at specific energies. The emission as well as the absorption is therefore strongly energy-dependent, and light sources with tunable excitation provide flexibility for controlling optical absorption in the sample.
- Using optical excitations with well-defined light polarization enables the excitation of carriers with specific spin and/or valley quantum numbers determined by the optical selection rules in the crystal. This reveals important information on the spin and valley dynamics in the material.

material acts as a probe as we make use of the interaction of the optical excitations with the direct environment to investigate, for example, the magnetization of adjacent layers or detection of molecules in proximity[18].

The understanding of layered semiconductors allows new possibilities to be explored for applications in optics and electronics[19]. Research is not merely aimed at miniaturization of devices (ultimate thinness and low energy consumption). New device concepts are based on physical properties emerging in the 2D limit. Examples that motivate optical spectroscopy work in this field are the electron valley index for information storage[20–22], periodic quantum emitters in flexible membranes[23,24], tunable absorption up to 100% by a single monolayer[25–28] or electrically switchable 2D magnetism[29].

This Technical Review begins with an introduction to the optical properties of layered semiconductors, using the model system of transition metal dichalcogenide (TMD) semiconductors, together with fabrication methods for typical sample structures. Next, we discuss the equipment used for optical spectroscopy set-ups, commercially available systems and components assembled in a laboratory. The main focus is on techniques used to uncover the main optical transitions in TMD materials and how they are affected by the sample structure and the surrounding layers. We also discuss how to access spin and valley polarization effects using optical methods and opportunities for Raman scattering and second-harmonic generation (SHG).

Layered semiconductors

Transition metal dichalcogenides

Interlayer van der Waals forces are considerably weaker than intralayer covalent bonding, and this weakness makes a very large number of crystals exfoliable in monolayers[2,30] (FIG. 1). TMD monolayers consist of a hexagonally oriented transition metal layer covalently bonded with top and bottom chalcogen layers[31,32] (FIG. 1a). Multilayers are coupled by weak van der Waals forces, and their symmetry is given by the stacking order of the layers[33,34], in which the relative twist angle between layers is 0° or 60°. The symmetry of the electronic states in monolayers and multilayer crystals governs the optical selection rules for light polarization in emission and absorption[35,36] (FIG. 1b), as has been studied for several decades for semiconductor nanostructures[37]. TMDs such as MoS_2 occur in different phases with semiconducting or metallic properties; here, we focus on the semiconducting phase (2H). The electronic and optical properties of TMDs change enormously as their thickness is reduced from bulk to atomic bilayers and monolayers. Bulk and few-layered TMDs have an indirect bandgap, whereas monolayers have a direct bandgap. This direct bandgap leads to strong photoluminescence (PL) emission[38,39] and also to a large, tunable optical absorption in monolayers[40,41]. The light–matter interaction is dominated by excitons, and this interaction is strongly enhanced when the incoming electromagnetic wave is resonant with the energy of the excitonic states[42].

The binding energies of excitons in TMD monolayers are of the order of several hundreds of millielectronvolts because of their large electron and hole effective masses[43], the reduced dielectric screening and the spatial confinement of the carriers within the monolayer. As a result, excitonic effects dominate the optical properties even at room temperature and beyond[44–47]. A strong spin–orbit splitting of about 200 meV (for Mo-based TMDs) and 400 meV (W-based) appears in the valence bands at the K point of the Brillouin zone in reciprocal space[43,48,49]. As a consequence, two separate interband optical transitions are observed in absorption, named A (transition from the upper valence band) and B (transition from the lower valence band)[32].

Interestingly, the strong Coulomb interaction is extremely sensitive to the dielectric screening associated with a spatially inhomogeneous environment[50,51]. This implies that the exciton transition energy and, to a larger extent, both the exciton binding energy and the free carrier bandgap can be tuned by engineering the local dielectric environment[52,53]. However, a possible undesirable consequence is that local dielectric fluctuations from disorder and impurities can result in strongly broadened optical transitions[54,55].

Optical transitions that are dipole-, momentum- and spin-allowed are referred to as 'bright', and the excitons recombine by emitting a photon. In layered materials, excitons with different spatial orientations of the optical dipole, either in-plane or out of the layer plane (see scheme in BOX 1), participate in optical transitions in WSe_2 (REF.[56]) and $InSe_2$ (REF.[57]), for example. Taking into account also optical transitions that rely on phonon absorption or emission or spin-mixing of the different electronic states results in a large number of possible bright and dark optical transitions for a specific material. The emission and detection efficiency for a specific optical transition can be optimized in applied magnetic fields and by selecting a particular light polarization and propagation direction[58–60]. These different types of optical transition can be addressed selectively in the optical microscope set-up. Mainly the interband transitions between the valence band and conduction band are probed, but transitions between excitonic states[61]

Multilayers
Structures consisting of more than one layer.

Excitons
Coulomb-bound electron–hole pairs.

Bright and dark optical transitions
A spin- and dipole-allowed transition is 'bright' whereas a spin- and/or dipole-forbidden transition is 'dark'.

Heterobilayers
Lateral or vertical heterojunctions formed by combining two different monolayers.

Moiré effects
Effects related to the interference pattern produced by the superposition of two slightly different lattice constants and/or twist angles.

Reconstructions
Spontaneous translational or angular rearrangements of atoms within multilayers, aiming for a lattice configuration with the lowest energy.

or intersubband transitions in multilayers can also be observed[62].

When the electron and hole reside within the same layer, we speak of intralayer excitons (FIG. 1c). By contrast, interlayer excitons can form in TMD heterobilayers with type-II (or staggered) band alignment[63], which have photoexcited electrons and holes residing in different layers (FIG. 1c,d). These excitons are referred to as indirect in real space. The difference in the lattice constants and twist angle between the monolayers forming the heterobilayer affects the alignment of K points, which determine whether the interlayer transition is direct or indirect in reciprocal space. In the indirect case, a phonon is needed in addition to a photon in the emission process[64,65]. The twist angle can also lead to the formation of moiré effects or to a local rearrangement of the stacking order (reconstructions), depending on the lattice mismatch between the stacked monolayers[14,66–68]. Note that confinement in nanometre-sized moiré potentials results in a spreading in k space of the carrier wavefunction. A moiré potential is a periodic modulation of the electron and hole band structure that depends on the difference between the lattice constants and/or twist angle.

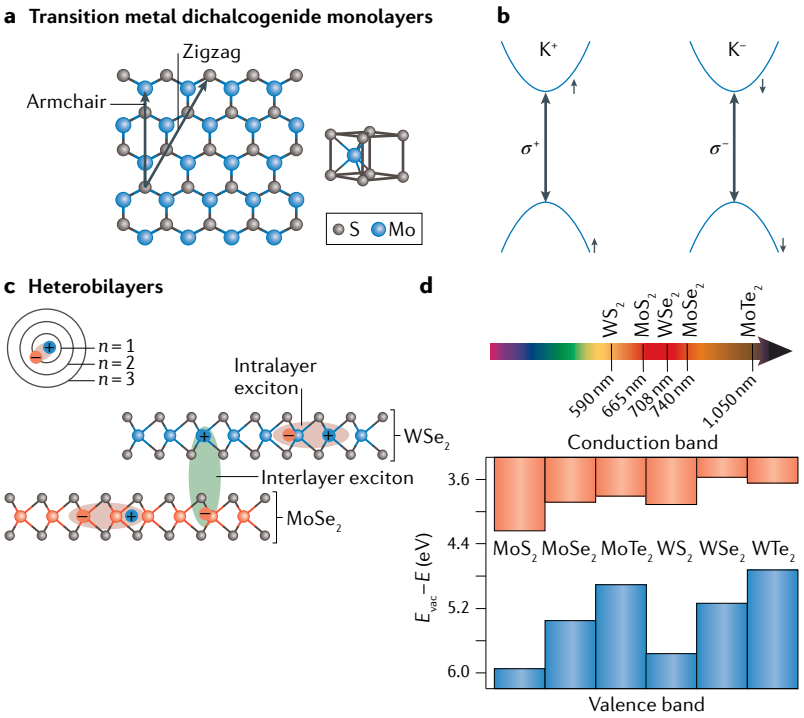

Fig. 1 | **Excitons in transition metal dichalcogenide monolayers and heterobilayers for optical spectroscopy. a** | Top view of MoS_2 monolayer hexagonal crystal structure. Here, transition metal atoms are shown in blue, chalcogen atoms in grey. **b** | Schematic illustrations of valley-selective optical transitions that obey chiral selection rules addressed optically using σ^+ (σ^-) polarized light[35,203–206]. The direct bandgap is at the K points of the Brillouin zone for transition metal dichalcogenide monolayers. **c** | Schematic of van der Waals heterobilayers. The individual monolayers show intralayer excitons (orange oval): each exciton is a bound pair of an electron and hole that resides in a single layer. Interlayer excitons can be found in heterobilayers, where the two charge carriers are located in different layers (green oval). Inset shows the hydrogen-like exciton states that correspond to different energy levels, designated by their principal quantum number n. **d** | Band alignment between 2D semiconductor monolayers calculated in REF.[63]. Arrow shows the wavelength of the optical gap for different materials varying from the visible to near-infrared. E_{vac}, vacuum energy. Panel **d** adapted with permission from REF.[63], AAAS.

The depth and periodicity of the moiré potential can generate localized emitters (trapping of individual excitons) or collective excitations (trapping of a critical number of excitons, generating interactions)[36], recently investigated using optical spectroscopy[4,69,70]. This approach for generating periodic, nanoscale potentials can certainly be extended to van der Waals heterostructures with different materials.

Monolayers and heterostructures

Widespread fabrication methods of monolayer samples on common SiO_2/Si substrates include mechanical exfoliation from bulk crystals (top-down) and bottom-up chemical vapour deposition (CVD). Promising high-quality monolayers are also obtained by molecular beam epitaxy[71,72].

Exfoliated TMD crystals from high-quality bulk materials commonly show defect densities of around $10^{12}\,cm^{-2}$ (REF.[54]), which is considerably larger than in III–V semiconductor nanostructures. Currently, the impact of defect concentration and type on the luminescence efficiency is being widely investigated, with improvements reported for samples treated with super-acids[73]. Exfoliation is widely used because of its simple handling even outside clean-room facilities and its cost efficiency. However, it has several limitations. The location of a single monolayer on the substrate is random, and searching for a monolayer among flakes of varying thickness is time-consuming. The monolayers are also small (the average lateral dimension is tens of micrometres), and the yield for finding monolayers per unit of surface area is low.

As an alternative to exfoliation, CVD allows direct growth of monolayer material on a large surface area[74–77]. With CVD, the monolayer dimensions and the number of monolayers per unit of surface area are considerably larger than for exfoliation (BOX 1), covering the entire substrate. It has been demonstrated that lateral as well as vertical TMD heterostructures can directly grow on flat or patterned SiO_2/Si substrates[78,79]. Detaching CVD-grown monolayer samples from the substrate to fabricate heterostructures is possible through water-assisted pick-up techniques[80,81]. Optical spectroscopy plays a critical role in characterizing these CVD-grown heterostructures, in particular non-uniform strain distributions in lateral heterostructures[82,83], unconventional polarization properties[84] and interlayer hybridizations[85] in commensurate heterobilayers, and moiré patterns in lattice-mismatched heterobilayers[13].

For both CVD-grown and exfoliated samples, the intrinsic quality can be evaluated by low-temperature optical spectroscopy (FIG. 2). Emission from defects and inhomogeneous broadening in the optical spectra can be used as diagnostic tools. In addition to the intrinsic layer quality, the impact of the underlying substrate can also limit the optical quality. This has been demonstrated by comparing low-temperature optical spectra between TMD monolayers (both CVD and exfoliated) on SiO_2 and encapsulated with hexagonal boron nitride (hBN)[16,55,86]. It is possible to further improve the optical response (in terms of signal strength for a particular transition) by optimizing the thickness of the top

Box 1 | **Description of a typical microscope for optical spectroscopy**

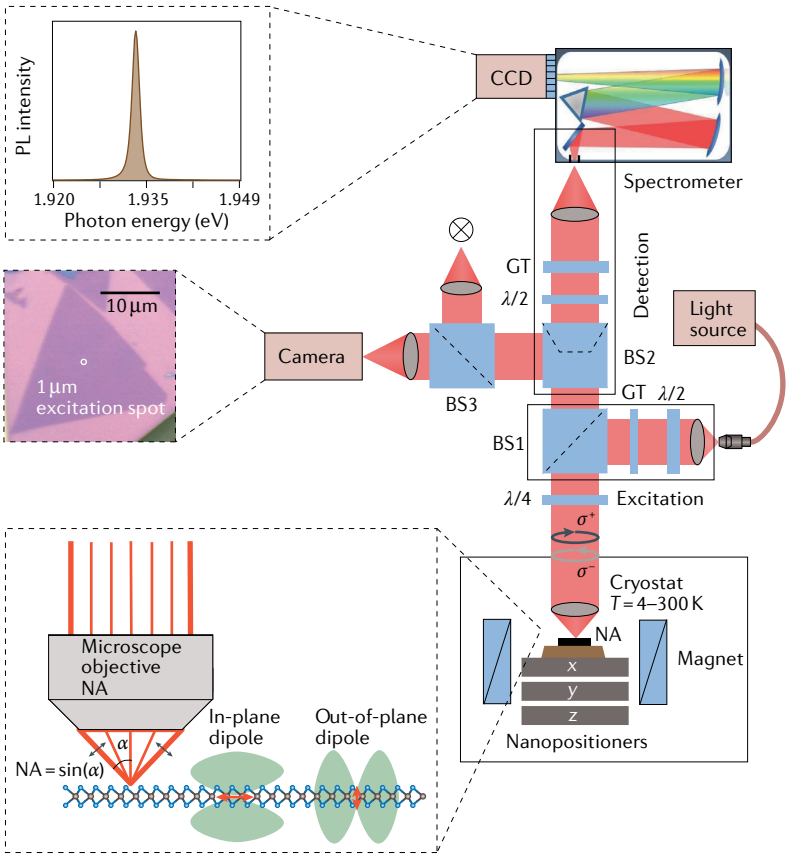

Micro-photoluminescence and reflectivity set-ups have to fulfil several key criteria: high spatial resolution for sample mapping and accessing specific sample areas, high detection efficiency (for example for quantum emitters in layered materials), and a combination of two detectors — one camera (charge-coupled device (CCD) or complementary metal–oxide–semiconductor (CMOS)) for sample imaging to guide the experiment, and another camera to accumulate the emission signal as a function of wavelength. All this can be combined in a microscope, where excitation and detection pass through the same objective (epifluorescence geometry). The spatial resolution is given by the diameter Δ of the detection spot. This depends on the numerical aperture (NA) of the objective and the wavelength λ through the Rayleigh criterion as $\Delta = \frac{0.61\lambda}{NA}$ (REF.[208]), where NA > 0.8 is common in commercial objectives. Excitons in layered materials can have an optical dipole either in-plane or out-of-plane (see inset representing emitters with in-plane and out-of-plane optical dipoles). Objectives with high NA also collect part of the emission from an out-of-plane optical dipole. A typical microscope set-up can be used to perform photoluminescence (PL), reflectance, photoluminescence excitation, Raman scattering and second-harmonic generation (SHG) spectroscopy experiments, all with similar equipment.

Van der Waals heterostructures of different materials can be studied for temperatures $T = 4$–300 K. The samples are placed on non-magnetic nanopositioners (travel distance of several millimetres). An objective located inside a cryostat is more stable for long signal integration times. The other microscope components remain at room temperature. The microscope design has several modules. The excitation light propagates through an optical fibre via the lower horizontal arm. The upper horizontal arm consists of a camera and broadband light source for sample imaging. The vertical arm is used for detection. The signal is collected by a spectrometer (here we show a Czerny–Turner geometry) with a diffraction grating coupled to a highly sensitive Si-CCD camera. Optionally, an optical fibre can be used in the detection path. The fibre transports the signal from the microscope to the spectrometer entrance and also acts as a spatial pinhole, making this a confocal arrangement for increased lateral (*xy*) and depth (*z*) resolution[209]. Polarization analysis is a key motivation for studying layered materials such as transition metal dichalcogenides for spintronics and valleytronics. Both linear polarization and circular polarization analysis can be achieved. For example, in the excitation part, a Glan–Taylor (GT) polarizer and a half-wave plate ($\lambda/2$) can be inserted. It is important to take into account the impact of the beamsplitters (BS) on the polarization state. The quarter-wave plate ($\lambda/4$) transforms the linear into circular polarization and vice versa. Instead of a simple wave plate, a liquid crystal retarder (where a precise retardance of $\lambda/2$, $\lambda/4$ and so on can be adjusted by the applied bias) can optionally be used in the detection path. This avoids a macroscopic beam movement that can occur during rotation of a typical wave plate as the retardance or polarization is changed. The performance of all optical set-up components is wavelength-dependent, such as limited bandwidth of reflection coatings, chromatic aberrations of the objective or optical retardance for specific wavelengths. Examples of optical components and polarization analysis (or polarization rejection) used in a microscope can be found in REFS[209–211].

and bottom hBN in encapsulated TMD samples (FIG. 2b, bottom panel)[87–89].

Individual layers from high-quality bulk crystals of different layered materials can be assembled into van der Waals heterostructures by using deterministic dry stamping[90] or direct pick-up[91]. This allows controlled transfer of layers at precise locations on the substrate. An optical micrograph of a van der Waals heterostructure is shown in FIG. 2a. During the transfer, micro-bubbles (blisters) due to trapped air, water or hydrocarbons can appear[91]. Agglomeration of the bubbles can be achieved by thermal annealing, which leaves clean and smooth

areas on the sample. In layered TMDs, the presence of bubbles or wrinkles can introduce defect emission due to strain and/or carrier localization. This can lower the optical transition energy and lead to the appearance of spatially localized emission (FIG. 2b).

Charge impurities from a disordered substrate or adsorbates can introduce charge potential fluctuations, which affect the optical properties. This is commonly observed in TMD monolayers on SiO_2/Si. As a result, transitions corresponding to charged exciton states (trions) can be detected in low-temperature PL (FIG. 2b,c). Independent control of the carrier density in gated field-effect devices[92,93] is thus crucial to study the optical properties in the charge-neutral, p- or n-doped regimes[92,94].

Optical properties

The fundamental optical transitions in TMDs lie in the energy range from about 1.1 eV (monolayer $MoTe_2$) to about 2.1 eV (monolayer WS_2) (FIG. 1d). Ferromagnetic semiconductors such as $CrBr_3$ and CrI_3 cover similar transition energies[95,96]. Interlayer excitons in heterostructures such as MoS_2/WSe_2 can reach emission wavelengths above 1,100 nm (<1.1 eV), approaching the telecommunication bands[97]. Black phosphorus is a layered semiconducting material with a direct bandgap

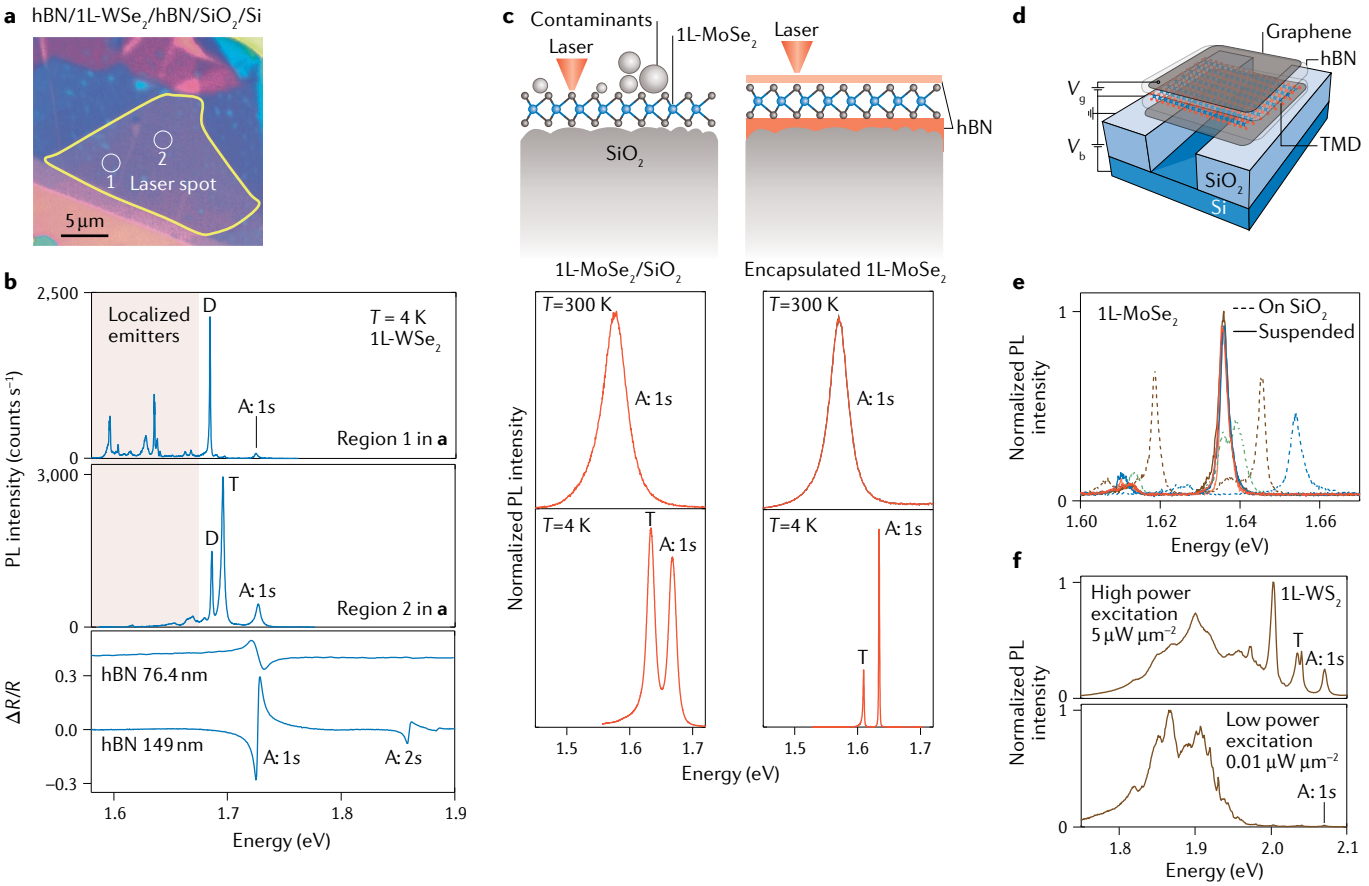

Fig. 2 | **Variation in photoluminescence response for different experimental conditions. a** | Optical micrograph of a typical van der Waals heterostructure sample containing a WSe_2 monolayer (1L) between the hexagonal boron nitride (hBN) top and bottom encapsulation layers. Sample homogeneity and sample imperfections (bubbles and wrinkles) can be seen. The non-homogeneous and homogeneous regions of the sample are labelled 1 and 2 in white, respectively. **b** | Typical photoluminescence (PL) spectra at $T = 4$ K recorded at locations 1 and 2 of the sample shown in **a**. The main exciton transitions are neutral excitons (A:1s), charged excitons (T) and the spin forbidden dark excitons (D). A:1s and T are quenched and localized emitters appear when PL is recorded on the bubbles or on wrinkles. However, strong PL emission corresponding to the main excitons from WSe_2 monolayers is recorded on the flat region of the sample. In the bottom panel, differential reflectivity ($\Delta R/R$) spectra of WSe_2 are compared for two different bottom thicknesses of hBN. The reflectance contrast varies for different hBN thicknesses owing to thin-film interference effects; thus, excited states (A: 2s) can be observed in optimized samples. **c** | Sketch of $MoSe_2$ monolayer sample structures in different dielectric environments. The left panel is the sample structure of a non-encapsulated transition metal dichalcogenide (TMD) monolayer on SiO_2; the right panel shows the TMD monolayer encapsulated in hBN. Typical PL spectra recorded at room temperature and at cryogenic temperature for the encapsulated and the non-encapsulated sample are shown in the bottom panels. The linewidth reduces substantially for the encapsulated sample at $T = 4$ K compared with the non-encapsulated sample. **d** | hBN-encapsulated $MoSe_2$ layer suspended over a trench[93]. **e** | Corresponding spectra for **d**. The PL emission energy remains constant in suspended samples on different locations of the monolayer, showing sample homogeneity[93]. **f** | WS_2 monolayer encapsulated in hBN on SiO_2/Si substrate, treated with Ar-plasma to generate optically active defects. Typical PL emission spectra for continuous-wave laser (532-nm) excitation at 0.01 µW and 5 µW at $T = 4$ K. The PL emission intensities of the main excitons are clearly visible at high power density, whereas these features are almost undetectable at low laser power density. PL spectra at low laser power density reveal that carriers can be trapped efficiently by defect sites and recombine by emitting photons at lower energy. Therefore, at low laser power, the PL emission of defects is considerably stronger than the free exciton emission. V_g, gate voltage; V_b, bias voltage. Panels **d** and **e** adapted with permission from REF.[93], APS.

that strongly varies with the number of layers and covers the visible (monolayer) to mid-infrared (bulk) spectral region[98]. The same evolution of bandgap change versus thickness occurs in $PtSe_2$ (REF.[99]), but here the bandgap is indirect as for Si; this is not efficient for emission but can be applicable for detectors. At the opposite end of the spectrum, layered hBN has a bandgap in the deep ultraviolet at 6 eV (200 nm)[100]. Graphene is a gapless material in its native state, but a finite gap of typically up to 0.1 eV can be opened when single-layer graphene is coupled to another material such as hBN through van der Waals coupling[101]. A tunable gap from 0 to 0.2 eV can be obtained by applying an out-of-plane electric field in bilayer graphene[102]; therefore, infrared spectroscopy can be used to study similar systems. Below, we describe the working principles of experiments to study absorption and emission of the optical transitions in layered semiconductors. The optical spectroscopy techniques discussed broadly in this Review are also applicable for the investigation of optical transitions in the energy range from infrared to ultraviolet. In this case, the experimental set-up shown in BOX 1 should be modified following a suitable selection of the optical components to match the material's transition energies.

Optical spectroscopy equipment

A typical spectroscopy set-up contains a light source and several optical components to guide the excitation light to the sample and the signal to the spectrometer (monochromator) and detector. A charged-coupled device (CCD) or a complementary metal–oxide–semiconductor (CMOS) camera is also essential for the sample imaging. In this section, we outline the characteristics of the main components and explain in BOX 1 the working principle of a versatile microspectroscopy set-up, widely used in commercial and also home-built systems.

Light sources

The main parameters for the laser excitation depend on the type of experiment and the sample's band structure. The wavelength is selected according to the optical transitions of interest, and the laser can be continuous-wave or pulsed. Pulsed lasers are more suitable in time-resolved experiments for better resolution in the time domain. For femtosecond or picosecond pulse duration, the spectral width of the excitation pulse should be taken into account when investigating transitions closely spaced in energy. At the same time, the laser peak power should be calculated to avoid sample damage. Owing to the small lateral dimensions of many exfoliated samples, high beam quality (aiming for perfect collimation, with low M^2 factor) lasers are required for focusing the beam tightly to a diffraction-limited spot. For continuous-wave excitation, laser diodes can be typically selected between 375 nm and 2,000 nm. For experiments requiring tunable wavelength excitation, convenient solutions for the 700–1,000-nm range include titanium sapphire (Ti:sapphire) lasers[103], which can be either pulsed (picosecond or femtosecond) or continuous. To cover the two wavelength ranges between 500–700 nm and 1,000–1,600 nm, an optical parametric oscillator can be coupled to the Ti:sapphire laser combined with a doubling crystal. Dye lasers can also be used, where the choice of dye and its solvent allows selection of the emission range. Absorption or reflection measurements are performed using a broadband white-light source to cover the full visible wavelength range. Often a simple halogen lamp suffices. When only one specific optical transition is investigated, a monochromatic light-emitting diode (LED) or superluminescent diode with 10–20-nm spectral bandwidth can be used. This enables a good compromise between a small spot size and sufficient excitation power. Other solutions include laser-driven light sources or super-continuum white lasers[104] that allow one to select a broad or narrow wavelength range for excitation, which makes them versatile for PL but also for broadband absorption experiments.

Optical components

The optical components used in the set-up are selected for a specific wavelength range depending on both the excitation source and the emission wavelength. These include the polarization components, microscope objectives and lenses (ideally achromatic doublets) shown in BOX 1. Homogeneous areas (flat surface, no charge fluctuations) in typical exfoliated samples have lateral dimensions down to a few micrometres. Therefore, small excitation/detection spots close to the diffraction limit are crucial to record spectra with transition linewidths limited by the homogeneous, not inhomogeneous, broadening. A diffraction-limited spot diameter (defined in BOX 1) can be achieved by using objectives with high numerical aperture (NA).

Detection

The final target is to detect the intensity as a function of wavelength of the light emitted from or scattered by the sample. The signal is focused on the entrance slit of a spectrometer, which can host different diffraction gratings. The collected signal is then dispersed by a diffraction grating, where a small (large) number of lines per millimetre on the grating allows the study of a broad (narrow) spectral range. The signal can then be detected by a CCD or high-quality CMOS chips. Alternatively, the spectrometer can be omitted and a simple combination of filters can be used in front of the detector.

Experimental conditions

Control of the ambient conditions is crucial. Many experiments are carried out at room temperature, but low-temperature experiments are necessary to access particular optical transitions. In simple bath cryostats, the sample is kept in thermal contact with a liquid helium bath at $T = 4$ K, either through helium exchange gas or a cold finger. The main drawback is that the bath needs to be periodically refilled with liquid helium. Alternatively, closed-cycle cryostats liquefy the helium gas using external compressors and allow continuous operation. In this case, the external compressor needs to be mechanically decoupled from the sample space to minimize vibrations. A piezo-based three-axis stage with nanometre step-size is used to place a specific area of the layer of interest in the focal point of the

M^2 factor
Represents the degree of variation of a beam from an ideal Gaussian beam. This factor reflects how well a collimated laser beam can be focused to a small spot, or how well a divergent laser source can be collimated.

objective. For high mechanical stability of the set-up, a low-temperature-compatible microscope objective can be placed inside the cryostat (BOX 1).

The sample holder can also be placed inside the bore of a superconducting coil to apply magnetic fields. In this case, the nanopositioners as well as the objective lens must be made of non-magnetic materials such as titanium and beryllium copper. The sample needs to be placed at the centre of the coil, which, in practice, limits the sample size and also the optical access (beam diameter). Magneto-optics can be used to extract the valley Zeeman splitting and hence identify the origin of new excitonic transitions, including interlayer excitons in TMD homo- and heterobilayers, trilayers and bulk[105,106]. It can also be used to investigate valley polarization dynamics and 'brightening' of otherwise spin-forbidden transitions[107]. Attention should be given to undesired Faraday effects in certain optical components. Magnetic ions in the glass result in an undesired rotation of the linear polarization in the presence of magnetic fields. This needs to be compensated by other polarization control elements[108].

Measuring absorption and luminescence

Absorption spectroscopy

Strictly speaking, measuring absorption (A) requires the measurement of both transmittance (T) and reflectance (R) where $A = 1 - R - T$. Transmission measurements require a transparent substrate and a detection path different from the excitation path, for example a separate microscope objective on each side of the sample or alternatively one objective combined with a fibre on the other side of the sample[109]. In practice, reflectivity is often measured, as it is the simplest experiment for samples on substrates such as SiO_2/Si that are not transparent. To get a quantity independent of the optical response of the set-up, one generally measures the reflectivity contrast defined as $(R_{sam} - R_{sub})/R_{sub}$, where R_{sam} is the intensity reflection coefficient of the sample with the TMD layer and R_{sub} comes from the same substrate without the TMD layer.

The optical properties of a material can be seen in a simple classical picture as the interaction between light (electromagnetic radiation) and various types of oscillator[110]. In TMD monolayers, the dominating oscillators are exciton resonances. In reflectivity measurements, different exciton resonances are accessible up to room temperature as they possess strong oscillator strength and high density of states. This allows one to observe the Rydberg series of the A-exciton: 1*s*, 2*s*, 3*s*… (FIG. 2b, bottom panel). Absorption spectroscopy gives a direct measure of the exciton resonance energy. To determine the exciton binding energy from reflectivity measurements, one must identify the energy position of both the exciton resonance and the free-particle bandgap. This is a challenging process given that multiple reflections caused by the sample and substrate interfaces can affect the spectral lineshape and subsequently the determined transition energies and absolute absorption (see details below). The exciton resonance energy, the absolute absorption and the relative oscillator strength can be precisely obtained from the reflectivity contrast using Kramers–Kronig relations[110,111], but these require a very clean spectral background subtraction. After identifying the series of excited exciton states and extrapolating the energy to the onset of the (quasiparticle) bandgap, the free-particle bandgap energy can be approximated. Magneto-absorption measurements also allow clear observation of higher exciton states, 4*s* or above. By fitting the transition energies as a function of the magnetic field, it is possible to extract the exciton binding energy and also the reduced exciton mass[45,109]. Other optical transitions related to defect states in the gap or other exciton complexes that possess weaker oscillator strength and/or comparatively lower density of states are difficult to trace in absorption, although they might appear in PL emission, as discussed below.

Monolayers. The energy of the A-exciton transition in TMD monolayers is given by the difference of the quasiparticle bandgap (of unbound electrons and holes) and the exciton binding energy. Engineering the dielectric environment (and hence all energy scales linked to the Coulomb interaction) results in changes in the quasiparticle bandgap[53] and the exciton binding energy of TMD monolayers. But the shift in the global A-exciton transition energy is rather small, as changes in quasiparticle bandgap and the exciton binding energies partially compensate each other. Compare FIG. 2c for monolayer $MoSe_2$ transition energies with and without hBN encapsulation, which are very close in value. However, the linewidth in absorption is strongly affected by dielectric disorder[86]. For instance, bubbles, wrinkles, polymer residues and hBN have different dielectric constants. Therefore, a non-uniform dielectric environment affects the energy of the exciton transitions and the overall shape of reflectivity spectra. Uniform dielectric slabs such as thick (tens to hundreds of nanometres) hBN layers can be exploited to steer the absorption. The visibility of exciton resonances in absorption is mainly influenced by the thickness of hBN and SiO_2 (FIG. 2b). This is due to thin-film interference effects; the bottom hBN thickness determines how far the monolayer is from the Si/SiO_2 interface, which acts as a mirror. The choice of hBN thickness can be optimized by using a transfer matrix approach to increase the visibility of the targeted transitions[88]. In this process, the particular energy of the excitonic resonance of the layered semiconductor should be taken into account[88]. Recent results in TMD materials placed in front of mirrors show a modulation in the absorption strength of up to 100% due to interference/cavity effects[25–28]. The strong influence of the dielectric environment on the light–matter interaction of atomically thin semiconducting membranes motivates potential sensing applications, including new device architectures with precisely tunable optical properties.

Multilayers. In general, the nature (direct or indirect) and the energy of the bandgap evolves as a function of the number of layers for a given material. In addition, the absorption of layered semiconductors such as black phosphorus[98] and $ReSe_2$ (REFS[112,113]) reveals information on the crystal structure of these particular materials as they are highly anisotropic in the layer plane (unlike the

Quasiparticle bandgap
Bandgap of free electrons and holes; the exciton resonance energies lie in energy below the quasiparticle bandgap.

more common TMDs such as MoS_2 and WSe_2), and different effects such as directional current flow or polarized excitons can appear in these cases. In few-layered TMDs and even in the bulk, strong excitonic features are reported even at room temperature in early studies[32]. In addition to these features typically attributed to the intralayer A- and B-exciton, more recently the observation of interlayer excitons (formed by carriers in two adjacent layers) has been reported in absorption of bulk samples[105,114,115]. Absorption of interlayer excitons is also reported in homobilayers and homotrilayers of MoS_2 (REFS[116,117]). In these systems, the transition energy of the absorption can be tuned through the application of an electric field perpendicular to the layers (Stark shift) over 120 meV, and the interaction between interlayer and intralayer excitons can be investigated[68,106,118].

Photoluminescence spectroscopy

Luminescence experiments are widely used for studying the macroscopic optical properties of materials as well as their microscopic electronic excitation, for the evaluation of crystalline quality (presence of defects) and for testing new optoelectronic devices[119,120]. Luminescence is defined as a surplus of the electromagnetic radiation (light) emitted by a solid, in addition to its equilibrium radiation described by Planck's law. This surplus energy is transformed into detectable luminescence radiation. During the process of luminescence, the electrons are excited to higher-energy states (by a light source in the case of PL). Subsequently, the carriers relax in energy, for example through phonon emission, followed by photon emission. The succession of all relaxation and recombination events involved lasts a relatively long time, which is a key difference from other types of 'secondary' radiation: reflected light and scattered light (for example, Raman). Once the material is excited with a light pulse, the luminescence continues to decay for some time and can be recorded in time-resolved PL[119]; see a review on time-resolved spectroscopy[121] for technical details. These experiments are used for studying exciton dynamics such as the exciton lifetime. In addition to time-resolved PL (an incoherent technique, in which the phases of the incoming and outgoing light do not match, owing to real absorption in the material), important information can also be gleaned from coherent spectroscopy such as four-wave mixing and two-colour pump–probe experiments[41,121–123].

In absorption spectra, optical transitions with large oscillator strength and high density of states dominate. By contrast, the emission spectrum given in PL experiments can be dominated by other transitions, as these experiments probe the population of a state. Typically, optical transitions at lower energies are detected in PL as carriers relax towards these lower-energy states before radiative recombination. It is therefore instructive to compare emission with absorption spectra (measured in reflection geometry) as in FIG. 2b. For the material investigated, monolayer WSe_2, the main bright exciton transition (A: 1*s*) that dominates in absorption is not generally the strongest feature in PL emission, as electron–hole pairs can relax towards states lying at lower energy to recombine[58].

Sample temperature. At room temperature, the main transitions such as the A- and B-excitons in TMDs will be broadened by scattering with phonons (compare spectra at $T = 4$ K and 300 K in FIG. 2c). Carriers or excitons are mobile at high temperature, and defect potentials in the lattice with only shallow confinement energy will not act as efficient trapping sites. At low temperatures, phonon absorption is reduced, and the linewidth reveals the sample quality (inhomogeneous broadening versus homogeneous broadening[89]). This is illustrated in FIG. 2c. The spectral lineshape and main emission energy can change compared with those at high temperature. Carriers can get trapped at sufficiently deep defect potentials. Also, excitonic complexes with lower binding energy, such as trions, are stable at low temperature and contribute to the PL signal (see FIG. 2b,c,f for three different materials[41,55,124,125]).

Excitation power. Laser power plays an important role as it controls the number of photoexcited carriers. Strictly speaking, the power density (defined as the average power per unit area) is directly related to the photogenerated exciton density in layered semiconductors. It is inversely proportional to the square of the focused beam radius; thus, it is directly related to the numerical aperture of the objective lens and laser wavelength. Let us take an example of a sample with a finite value of defect density: for a tightly focused beam (spot size ~1 μm), at low laser power (typically hundreds of nanowatts) all carriers can be trapped at defect sites and the PL signal of free excitons is not visible, as in FIG. 2f (lower panel) where we can estimate the exciton density to be of the order of $10^5\,cm^{-2}$. Increasing laser power (few microwatts) fills all defect sites, and free-exciton PL can be measured in addition to defect emission (see FIG. 2f, upper panel, where the exciton density is now ~$10^8\,cm^{-2}$. Further increase in power (tens to hundreds of microwatts) will lead to such a high concentration of excitons that exciton–exciton interactions start to play a role. At high excitation density, very different phenomena such as biexciton formation and exciton–exciton annihilation can be studied depending on the material[126–129]. Understanding emission for high exciton (carrier) concentrations is crucial for applications such as lasing and for investigating collective states such as condensates[70,130].

Sample quality and dielectric environment. Two monolayer samples exfoliated from the same high-quality bulk crystal but placed on different substrates can exhibit very different PL characteristics (see FIG. 2c for a comparison of $MoSe_2$ on SiO_2 and on hBN, respectively). The total line broadening comes both from homogeneous contributions given by ~1 ps lifetime (below 1 meV linewidth) and from inhomogenous contributions from sample imperfections (impurities, defects, interface, substrate and so on)[122]. The key role of high-quality hBN buffers with low defect density is to provide atomic flatness[131] for monolayer deposition and a very clean, homogeneous dielectric environment. The hBN bulk bandgap of 6 eV (REF.[100]) is high enough to use hBN flakes as an essentially transparent encapsulation

Homobilayers and homotrilayers
Stacking of two and three monolayers of the same material, respectively.

Four-wave mixing
Nonlinear effect arising from the third-order optical nonlinearity where one or two new wavelengths are produced by interactions between two or three wavelengths. Four-wave-mixing microspectroscopy accesses coherence and population dynamics of excitons.

Two-colour pump–probe experiments
Pump–probe experiments using two distinct laser beams where the wavelengths of the pump and probe beams are not identical.

layer for many materials, providing an ideal environment to address intrinsic properties of 2D-TMDs and preserving good optical quality in air-sensitive materials such as CrI_3 or black phosphorus. As the inhomogenous broadening is largely suppressed in high-quality samples of TMD monolayers, the linewidth starts to be an indication of the exciton lifetime (homogeneous broadening) and can be tuned by carefully choosing the encapsulating hBN thickness so as to place the monolayer on a node or anti-node of the electromagnetic field in the multilayer structure[89].

PL emission is sensitive to the presence of wrinkles or bubbles, which generate strain and localization potentials in encapsulated monolayers. Small strain (1%) in a monolayer induces a large (about 50 meV) shift in bandgap energy[132], which can explain shifts in absolute emission energy from sample to sample and for different areas of the same sample. Therefore, in practice, PL emission intensity as well as linewidth varies on different locations of TMD monolayers (see FIG. 2b when the detection spot, 1 μm in diameter, is scanned across a WSe_2 monolayer). Remarkably, exciton emission energy that does not vary as a function of the detection spot position has been observed in hBN-encapsulated $MoSe_2$ monolayers suspended over a trench[93] (see FIG. 2d,e), indicating a homogeneous (in terms of dielectric constant), inert environment.

The general study of the dielectric environment, surface quality, flatness, charging events and their impact on optical properties is also important for other nanostructures such as carbon nanotubes[133–137] and layered perovskites[138], which show strong excitonic effects.

Interference effects. Layered materials are usually placed on a substrate such as Si with an SiO_2 layer of typically 85 nm. As discussed earlier for white-light absorption experiments, optical interference will also be important for the laser excitation beam and the PL emission as a function of the SiO_2 thickness and possibly the encapsulation layer thickness. Conversely, for constant SiO_2 thickness, absorption and emission intensities and directivity will depend on the wavelength, as detailed in REFS[87,139]. In practice, the thickness of the SiO_2 layer on top of Si is chosen to maximize optical contrast of monolayers during sample fabrication, as discussed in detail for graphene on SiO_2 (REF.[140]).

Emission dynamics. The detected luminescence signal from a layered semiconductor is the result of an intricate interplay between radiative and non-radiative energy relaxation. Time-resolved PL can be performed by using a pulsed laser excitation and measuring the recombination (emission) time; for a detailed introduction to time-resolved spectroscopy, see REF.[121]. In clean TMD samples, the strong exciton oscillator strength leads to an intrinsic radiative lifetime of the order of 1 ps at low temperature[141] for free excitons. Spatially localized excitons recombine considerably more slowly than free 2D excitons and have a lifetime up to three orders of magnitude longer than the exciton's intrinsic radiative lifetime. Low-temperature measurements on high-quality samples allow each transition to be spectrally isolated (either with bandpass filters or with a spectrometer) and then the emission dynamics of each optical transition to be studied separately[89,124,142].

Optical dipole orientation. In TMD monolayers, the main optical transitions have an in-plane optical dipole. They therefore emit light normal to the monolayer plane. However, in addition to these bright (spin-allowed) transitions, excitons that have an out-of-plane optical dipole also emit light[58]. Out-of-plane dipole transitions are also prominent in InSe (REFS[57,143]). Because of the small sample dimensions, most experiments are carried out in a microscope with a high-NA objective (>0.8) (see inset on microscope objective in BOX 1). As a result, PL emission containing out-of-plane and also in-plane components in the monolayer is detected. In WSe_2 and WS_2 monolayers, dark excitons are prominent (FIG. 2b) and lead to exotic, higher-order complexes (such as biexcitons made up of a dark and a bright exciton, and dark trions[128,144]), which can be identified by monitoring the orientation of the exciton dipole. The role of out-of-plane dipole emission is also investigated for quantum emitters in WSe_2 (REF.[145]). Brightening of (spin-) dark states due to an increased mixing of the spin-states in WSe_2, WS_2, $MoSe_2$ and MoS_2 monolayers can be observed in low-temperature magneto-PL experiments by applying strong (ideally several tens of tesla) in-plane magnetic fields[59,60,146].

Multilayers. PL spectroscopy is also useful in studying TMD heterobilayers with type-II band alignment (FIG. 3). It can be used to examine spatially indirect interlayer excitons (FIGS 1c,3c) with large predicted binding energies (~ 150 meV)[65,147,148]. A long-period moiré pattern (see sketch in FIG. 3a) offers new directions to explore and control exciton arrays in twisted TMD heterobilayers from potentials that trap individual excitons to the formation of minibands. This allows physics related to correlated states[4], for potential applications in quantum optoelectronic devices[15,68]. Some key characteristics of interlayer excitons include a long lifetime (nanoseconds), a wide transition-energy tunability that ranges over several hundreds of millielectronvolts in applied electric fields (FIG. 3d) and a characteristic Zeeman splitting with different sign and amplitude compared with intralayer excitons[115].

Hybrid structures. A very active field of research is devoted to incorporating TMD materials into photonic cavities, plasmonic and dielectric meta-surfaces[149]. These structures will affect the recombination dynamics but also change the emission direction, which can be investigated by Fourier plane imaging[150]. In this case, angular information on the light scattered from the sample can be collected. For instance, this technique allows the measurement of the energy–momentum dispersion relation of the outcoupled light from nanostructures and the angular dispersion in cavities with strong light–matter interaction[151–154]. Imaging the Fourier plane of the objective lens is technically challenging, as this plane physically lies on the nearside of the metallic case of the objective housing. Therefore, relay optics is used

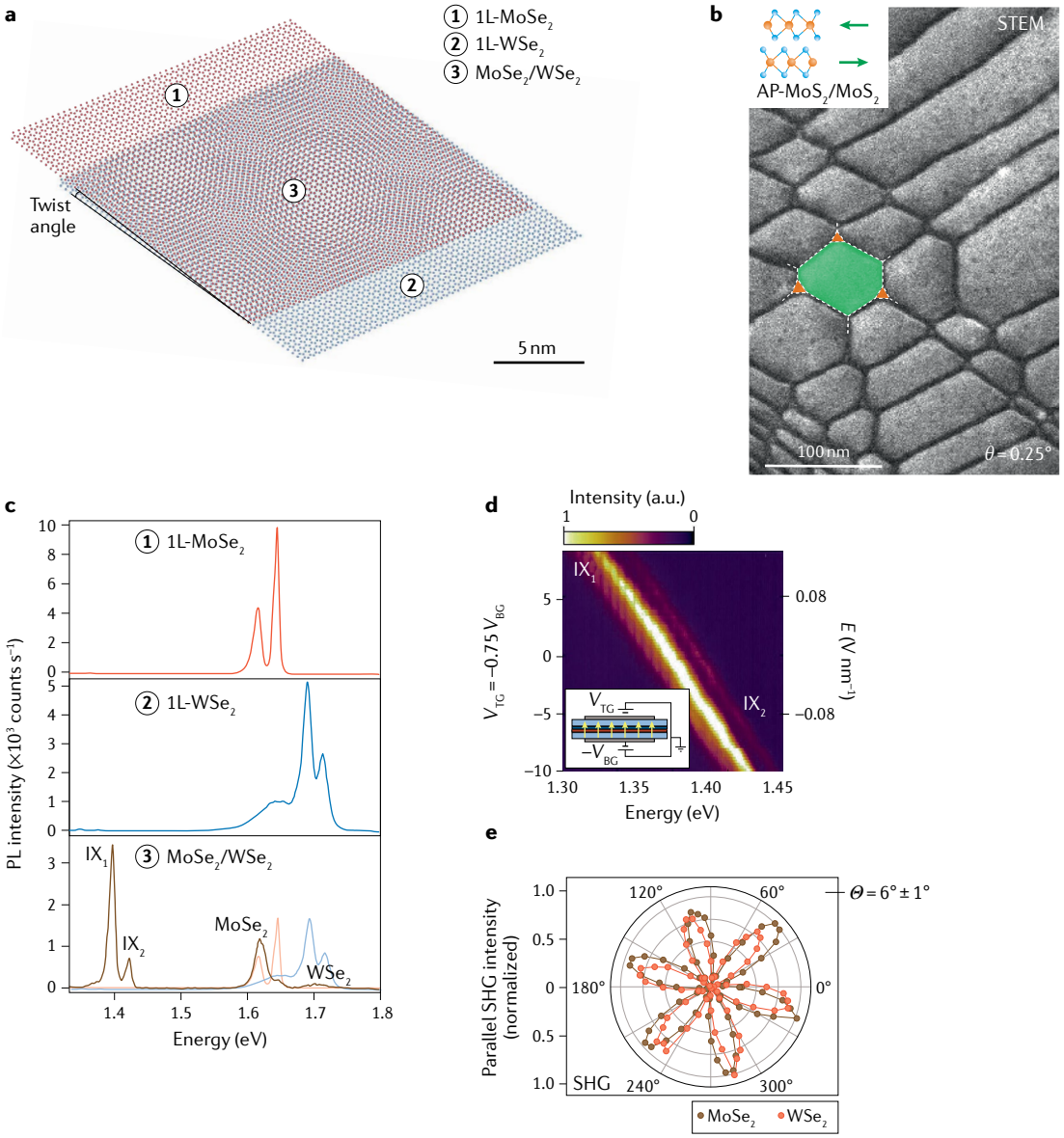

Fig. 3 | **Moiré interlayer excitons in heterobilayers. a** | Two different monolayer (1L) materials stacked vertically that display a moiré pattern owing to a slight lattice mismatch and twist angle. Different local atomic alignments in the heterostructure show different optical properties[4,36,161]. Three spots labelled 1, 2 and 3 are chosen for photoluminescence (PL) measurements on $MoSe_2$ monolayer, WSe_2 monolayer and $MoSe_2/WSe_2$ heterostructure, respectively, and corresponding spectra are shown in panel **c**. **b** | Scanning tunnelling electron microscopy (STEM) image of a reconstructed MoS_2 bilayer with a twist angle of 0.25° (REF.[67]). AP stands for anti-parallel and is indicated by green arrows. Colours highlight different types of domain, formed because of the interaction between the layers. **c** | Example of PL spectrum from a hexagonal boron nitride (hBN)-encapsulated $MoSe_2$ monolayer (solid red curve), WSe_2 monolayer (solid blue curve) and $MoSe_2/WSe_2$ heterostructure (solid black curve)[161]. Intralayer exciton emission is observed from the $MoSe_2$ and WSe_2 monolayers. The interlayer exciton emission (IX_1 and IX_2) appears in energy below the intralayer resonances from the heterostructure. **d** | Electrical control of interlayer excitons in a $MoSe_2/WSe_2$ heterobilayer. Colour map of PL emission spectra as a function of applied gate voltages V_{TG} and V_{BG} when sweeping at constant doping. Stark shift of the interlayer excitons in applied electric fields perpendicular to the layers indicates an out-of-plane electric dipole[161]. **e** | Polarization-resolved second-harmonic generation (SHG) intensity of the individual monolayers from a different publication compared with panels **c**,**d**, indicating the armchair directions of the monolayers that determine the twist angle (θ) between the WSe_2 and $MoSe_2$ layers[178]. Panel **b** adapted from REF.[67], Springer Nature Limited. Panel **c** adapted with permission from REF.[207], Dmitrii Unuchek. Panel **d** adapted from REF.[161], Springer Nature Limited. Panel **e** adapted from REF.[178], CC BY 4.0.

to project the Fourier plane of the objective lens to the imaging camera (see supplement of REF.[58]). The incoming laser beam must be focused onto the sample plane by a high-NA objective lens, and the backscattered light is collected with the same objective lens as shown for the set-up in BOX 1. The collected light is then passed through a combination of lenses and a pinhole and projected to the CCD.

Photoluminescence imaging

PL imaging is a powerful tool to access information about sample quality and to image the spatial diffusion of excitons far away from the excitation spot. This can be performed in the same set-up as shown in BOX 1 where the sample is excited with a tightly focused excitation beam on a diffraction-limited spot in the sample plane. The resulting PL is imaged by a cooled Si-CCD camera after the laser beam has been filtered out with an additional filter in the detection system[155–159]. Excitons with longer PL recombination times (which depend on temperature) can travel further, for example dark excitons in TMD monolayers or bright interlayer excitons in heterobilayers. Images for different polarizations of the emitted light (σ^+ and σ^-) give information on the diffusion of excitons or carriers associated with different valleys[158,159]. The shape and diameter of the PL image also provides information on sample quality and a varying in-plane potential landscape for excitons.

Photoluminescence excitation spectroscopy

In photoluminescence excitation spectroscopy (PLE), the PL emission intensity for a chosen transition energy is recorded for different photon excitation energies. Tunable lasers or powerful white light sources are used as an excitation source. The linewidth and tuning step of the light source will determine the spectral resolution of the PLE experiment. The measured PL intensity will depend on two factors: first, the absorption strength at the excitation energy, and second, the efficiency of energy relaxation from the state that absorbed to the state that lies at lower energy and emits light. This combined dependence on both absorption and energy relaxation (often through phonon emission) makes PLE spectroscopy an interesting tool for several investigations, detailed below.

Interlayer excitons and charge transfer. A PL signal enhancement of interlayer excitons is observed when the laser excitation energy is resonant with intralayer states in one of the layers. This signal enhancement confirms that interlayer excitons can form by charge transfer processes between the layers[65,160,161] (see FIGS 1d and 3c). In general, electronic coupling or charge transfer between layers can be investigated by tuning a laser in resonance with an electronic transition in one layer and monitoring PL emission at a transition energy corresponding to the adjacent layer or to the heterostructure as a whole.

Measuring excited exciton states. PLE can be also used to establish a link between optical transitions with similar microscopic origin within the same monolayer. In MoS_2 monolayers, B-exciton states energetically overlap with the excited A-exciton states (A: 2*s*, A: 3*s*…). PLE spectroscopy allows the excited states to be distinguished by collecting the emission intensity of the ground state, A: 1*s*, as a function of the excitation laser energy, scanned over the energy of A: 2*s*, A: 3*s* and so on. Besides states with *s*-symmetry, *p*-states can also be examined. To access *p*-states, two-photon absorption processes are necessary, and therefore the laser energy needs to be tuned to half of the transition energy[100]. The identification of high-excited exciton states in one- and two-photon PLE is a powerful method to evaluate the impact of different dielectric environments on the energy evolution of the exciton states. Furthermore, it is possible to extract the exciton binding energies[162] and investigate predictions on *p*-exciton state splitting[163]. However, one should note that the crystal symmetry or disorder effects can mix *s*- and *p*-exciton states[164,165].

Identification of dominant phonon modes for energy relaxation. In addition to key information on absorption, PLE is used to identify efficient relaxation channels. In PLE experiments on $MoSe_2$ monolayers, a periodic oscillation in energy is observed over an energy range without any expected exciton resonance (roughly constant absorption[166]). These maxima are all equally spaced in energy by longitudinal acoustic phonons at the M point of the Brillouin zone, LA(M), revealing the efficient energy relaxation of excitons through emission of LA(M) phonons[125,167]. This experimental observation was possible owing to the spectrally narrow excitation source, which could resolve fine separations between different peaks related to phonon emission[125,168].

Spin–valley polarization

For polarization analysis, linear polarizers and waveplates can be inserted in the detection and excitation path of the set-up (see BOX 1 for practical details). Exciting a system with polarized light can address a specific spin or valley state (FIG. 1b). The emitted light gives information on spin and valley dynamics in time-integrated PL experiments. The circular polarization, P_c, in time-integrated experiments depends on the exact ratio of PL emission time τ_{PL} to depolarization time (τ_{depol}) as $P_c = P_0 / (1 + \frac{\tau_{PL}}{\tau_{depol}})$, where P_0 is the initially generated polarization, which could depend on the excitation energy[169,170].

TMD monolayers

The interband transitions in monolayer materials such as MoS_2 are governed by chiral selection rules, as optical transitions in the K^+ (K^-) valley are σ^+- (σ^--)polarized (FIG. 1b). For neutral, bright excitons, the intrinsic lifetime is of the order of 1 ps at $T = 4$ K, so from time-integrated PL experiments that report P_c values of the order of 50%, one can infer that τ_{depol} is at least of this order of magnitude. In practice, more sophisticated pump–probe measurements reveal very short valley lifetimes for neutral excitons[122]. The ratio τ_{PL}/τ_{depol} can be tuned by placing monolayers in optical microcavities[171,172] or on top of a semimetal such as graphene[173]. Longer valley lifetimes in monolayers are reported for resident carriers (not excitons) as shown independently in several studies[20–22], measured with pump–probe techniques such as Kerr rotation used for probing polarization in semiconducting or metallic nanostructures[7].

TMD heterobilayers

Optical spectroscopy can be used to probe the local atomic registry: that is, how metal and chalcogen atoms are aligned in the top layer with respect to the bottom

layer[3,36,161]. The optical polarization selection rules will be modified according to the atomic registry affecting the spin–valley polarization mechanisms. From the optical selection rules, information can be gleaned on the formation of nanoscale, periodic moiré potentials (see sample sketch in FIG. 3a). But similar to bilayer graphene, reconstruction can occur when two TMD layers are brought in contact, which can be visualized using imaging techniques such as scanning transmission electron microscopy (STEM) or scanning electron microscopy (SEM) and conductive atomic force microscopy[174]. A STEM image showing lattice reconstruction in a twisted MoS_2 bilayer is presented in FIG. 3b. Recently, SEM images of hBN-encapsulated twisted WSe_2 bilayers have also been reported[14], showing that a spatially varying reconstruction pattern develops owing to the interaction between the respective layers after stacking. Polarization selection rules probed in PL also carry information on different stackings (H-type or R-type for 60° or 0° twist angle, respectively)[1,175]. Therefore, polarization-resolved optical spectroscopy together with direct atomic-resolution imaging of the lattice is a powerful combination for analysing the formation of moiré potentials[15]. The PL experiment samples a spot diameter of 1 μm, whereas moiré potentials can occur with a periodicity of nanometres (see FIG. 3a), which leads to averaging effects. The intrinsic lifetime of interlayer excitons is of the order of nanoseconds at low temperature (and not picoseconds as for intralayer excitons in monolayers), which allows for PL imaging of exciton and polarization spatial diffusion[148,158,159]. The physics of both intralayer and interlayer excitons can be accessed in the monolayer and bilayer regions of the same sample, as in FIG. 3a and c.

Experiments in applied magnetic fields

The circular polarization can be manipulated by applying external magnetic fields[176,177]. Interesting examples are heterobilayers, where a giant Zeeman splitting of 26 meV at $B = 30$ T for interlayer excitons induces near-unity valley polarization measured in PL emission[178]. In monolayer $MoSe_2$, a field of 7 T results in near-unity polarization of electrons probed in absorption and emission[179].

Crystal quality and orientation

Inhomogeneous broadening and low-energy emission in the PL optical spectra can be used as a diagnostic tool to identify the presence of defects. However, PL spectroscopy cannot provide information on the crystallographic orientation of monolayers with respect to the substrate edge or other monolayers (for example for layers with D_{3h} point-group symmetry). Furthermore, additional optical methods are necessary to assess the crystal quality of the material. Two powerful optical techniques are detailed below that can be used to analyse the crystal quality and orientation of samples.

Raman spectroscopy

Raman spectroscopy is based on the analysis of laser light scattered by a material. During this process, the crystal typically absorbs (or emits) energy in the form of lattice vibrations — phonons. The analysis of the scattered light's energy and polarization reveals information on the crystal symmetry and quality, doping and, where applicable, alloying and stacking in multilayers. A typical PL set-up (BOX 1) can be conveniently adapted to collect the Raman spectra by selecting a suitable set of filters according to the wavelength of the excitation laser. Typically, filters for Raman spectroscopy reject the excitation laser with a cut-off frequency of a few tens of cm^{-1} (~10 meV from the single mode energy). The selection of laser wavelength, λ, has an important impact on the spectral sensitivity, as the intensity of the Raman signal is proportional to λ^{-4}. Key parameters of the excitation laser include spectral linewidth (≤1 GHz) for high-spectral-resolution systems, frequency and power stability, spectral purity (side-mode suppression ratio ≥65 dB), beam quality (close to Gaussian) and output power. The excitation wavelength in the Raman scattering of TMDs is also important because of the presence of excitonic states. When the photon energy matches the transition energy of a real state, it gives rise to a strong signal enhancement and appearance of new features, associated with symmetry-dependent electron–phonon interactions (resonant Raman scattering)[180,181].

Information on the structural phase and composition of materials can be obtained by means of Raman spectroscopy[182]. An example is the currently debated link between ferromagnetic ordering and structural phase transitions in CrI_3 (REF.[6]) as a function of temperature. Raman spectroscopy can reveal anisotropy in the crystal structure of, for example, $ReSe_2$, which can be directly linked to measurements of anisotropic optical absorption in the same material[183]. Electron–phonon interactions can have strong effects on the Raman frequencies. As a result, doping effects can be effectively monitored in TMD monolayers, for example, with the out-of-plane phonon, A_1', owing to its strong electron–phonon coupling[184,185]. It is also possible to extract quantitative information about the presence of uniaxial strain, as the in-plane phonon energy, E', decreases with applied tensile strain, and a splitting occurs (degeneracy is lifted)[186]. An estimation of the monolayer crystal quality and presence of defects can be obtained owing to the activation of defect-induced zone-edge phonon modes, such as the LA(M)[187]. Furthermore, disorder and interference effects originating from the substrate affect the intensity and spectral shape of the optical phonons in the monolayer[188]. A powerful and reliable means to determine the number of TMD layers with atomic-level precision is to measure the energy difference between the two main vibrational modes (E and A phonons) affected by interlayer interactions[189]. Apart from the high-frequency (≥80 cm^{-1}) spectral range, the number of layers can be identified by collecting optical signatures of the rigid layer vibrations (breathing and shear modes) in the ultra-low-frequency range[190]. This requires the installation of a set of volume-Bragg filters that reject the elastic scattered light and give access to frequencies down to about 10 cm^{-1} (or about 1 meV) without the need of a triple monochromator. In this low-frequency case, important information on the interlayer interaction and determination of the stacking order in multilayers can be obtained[33]. In TMD multilayers, resonant Raman spectroscopy can also provide a fingerprint of

the extension of excitons over several layers, as otherwise symmetry-forbidden modes are activated for the so-called C-exciton region[181] in energy above the A- and B-excitons. Raman spectroscopy can also be used to investigate the competition between formation of periodic moiré potentials and local reconstruction (compare FIG. 3a and b) in artificially stacked $WSe_2/MoSe_2$ and bilayer MoS_2 as a function of twist angle[17,191].

Second-harmonic generation

SHG is a nonlinear optical process that converts two photons of the same frequency into one photon of twice the original frequency. It is a powerful technique for analysing the orientation and symmetry properties of 2D materials. For SHG experiments, the optical set-up is typically coupled to a pulsed laser that is capable of generating sufficient peak power for this nonlinear optical process. The SHG signal depends on the elements of the second-order susceptibility tensor $\chi(2)$ (REF.[110]), which are non-vanishing for non-centrosymmetric media (odd number of TMD layers) along the armchair direction of TMDs (FIG. 1a). This crystallographic direction can thus be directly determined by varying the linear polarization axis in the experiment. The resulting polar plot of the SHG intensity reveals the crystallographic orientation of the material, useful for precisely measuring the relative twist angles (stacking) of homo- and heterobilayers[192,193] (FIG. 3e). For SHG on heterostructures/multilayers, interference effects impacting the SHG intensity from different layers (such as hBN and different TMD materials) need to be considered and can be useful to distinguish between 0° and 60° relative crystallographic orientations[192]. New techniques can exploit this effect to map with high spatial resolution (~400 nm) the armchair orientation in twisted bilayers[194], as well as in large monolayer areas (>10^4 μm^2), and evaluate their crystal quality, as dislocations and grain boundaries can affect the armchair orientation, for example by changing the lattice vector[195]. Also, the presence of uniaxial strain can be quantified by measuring the SHG intensity along different polarization directions[196].

The SHG response of a material not only reflects the crystal structure but also depends on the electronic excitations[197]. The efficiency of the SHG signal can be enhanced by several orders of magnitude by selecting the excitation energy to be in resonance with excitonic states of the investigated materials[42]. This enables studying the role of electronic excitations (exciton resonances) on the SHG response of a material[198,199]. Using the sensitive SHG response to detect the energy position of electronic transitions is termed 'SHG spectroscopy'. In bilayer CrI_3, SHG has been shown to originate from the layered antiferromagnetic order, which breaks both the spatial inversion symmetry and the time-reversal symmetry[5] of this centrosymmetric crystal. This also makes SHG a highly sensitive probe for magnetic ordering in layered materials.

Challenges and outlook

The versatile optical spectroscopy techniques discussed here are important tools for uncovering optical properties of new materials from the large catalogue of layered compounds[2] that await investigation. Interesting technical developments in optical spectroscopy are underway with the main targets of improving spatial resolution[62], accessible wavelength range[100] and compatibility with other microscopy techniques. One of the future challenges is to image moiré potentials and perform spectroscopy on a particular local atomic registry that lies on the nanometre scale[36]. This will be important for understanding the origin of localized emitters and how optical properties depend on moiré periodicity. Nanometre-scale moiré superlattices can be imaged by using near-field spectroscopy techniques, SEM, atomic-resolution transmission electron microscopy, atomic force microscopy or scanning tunnelling spectroscopy[13,14,200,201]. One possible way to increase spatial resolution in optical spectroscopy below the diffraction limit is to perform tip-enhanced spectroscopy, as recently demonstrated[202]. In this technique, a nanometre-sized silver tip is scanned across a nanobubble in WSe_2 to locally enhance emission. PL spectra are collected by illuminating the tip by laser in a near-field scanning optical microscope.

Published online: 16 December 2020

1. Ubrig, N. et al. Design of van der Waals interfaces for broad-spectrum optoelectronics. *Nat. Mater.* **19**, 299–304 (2020).
2. Mounet, N. et al. Two-dimensional materials from high-throughput computational exfoliation of experimentally known compounds. *Nat. Nanotechnol.* **13**, 246–252 (2018).
3. Seyler, K. L. et al. Signatures of moiré-trapped valley excitons in $MoSe_2$/ WSe_2 heterobilayers. *Nature* **567**, 66–70 (2019).
4. Shimazaki, Y. et al. Strongly correlated electrons and hybrid excitons in a moiré heterostructure. *Nature* **580**, 472–477 (2020).
5. Sun, Z. et al. Giant nonreciprocal second-harmonic generation from antiferromagnetic bilayer CrI_3. *Nature* **572**, 497–501 (2019).
6. Ubrig, N. et al. Low-temperature monoclinic layer stacking in atomically thin CrI_3 crystals. *2D Mater.* **7**, 015007 (2019).
7. Mak, K. F., Shan, J. & Ralph, D. C. Probing and controlling magnetic states in 2D layered magnetic materials. *Nat. Rev. Phys.* **1**, 646–661 (2019).
8. Zhong, D. et al. Van der Waals engineering of ferromagnetic semiconductor heterostructures for spin and valleytronics. *Sci. Adv.* **3**, e1603113 (2017).
9. Ciorciaro, L., Kroner, M., Watanabe, K., Taniguchi, T. & Imamoglu, A. Observation of magnetic proximity effect using resonant optical spectroscopy of an electrically tunable $MoSe_2/CrBr_3$ heterostructure. *Phys. Rev. Lett.* **124**, 197401 (2020).
10. Lyons, T. P. et al. Interplay between spin proximity effect and charge-dependent exciton dynamics in $MoSe_2/CrBr_3$ van der Waals heterostructures. *Nat. Commun.* **11**, 6021 (2020).
11. Sortino, L. et al. Enhanced light–matter interaction in an atomically thin semiconductor coupled with dielectric nano-antennas. *Nat. Commun.* **10**, 5119 (2019).
12. Paik, E. Y. et al. Interlayer exciton laser of extended spatial coherence in atomically thin heterostructures. *Nature* **576**, 80–84 (2019).
13. Zhang, C. et al. Interlayer couplings, Moiré patterns, and 2D electronic superlattices in MoS_2/WSe_2 hetero-bilayers. *Sci. Adv.* **3**, e1601459 (2017).
14. Sushko, A. et al. High resolution imaging of reconstructed domains and moiré patterns in functional van der Waals heterostructure devices. Preprint at https://arxiv.org/abs/1912.07446 (2019).
15. Andersen, T. I. et al. Moiré excitons correlated with superlattice structure in twisted WSe_2/WSe_2 homobilayers. Preprint at https://arxiv.org/abs/1912.06955 (2019).
16. Shree, S. et al. High optical quality of MoS_2 monolayers grown by chemical vapor deposition. *2D Mater.* **7**, 015011 (2019).
17. Holler, J. et al. Low-frequency Raman scattering in WSe_2–$MoSe_2$ heterobilayers: evidence for atomic reconstruction. *Appl. Phys. Lett.* **117**, 013104 (2020).
A study that shows evidence of atomic reconstruction and stacking order in heterobilayers by means of low-frequency Raman spectroscopy.
18. Zhao, Y., Ippolito, S. & Samorì, P. Functionalization of 2D materials with photosensitive molecules: from light-responsive hybrid systems to multifunctional devices. *Adv. Opt. Mater.* **7**, 1900286 (2019).
19. Mak, K. F. & Shan, J. Photonics and optoelectronics of 2D semiconductor transition metal dichalcogenides. *Nat. Photonics* **10**, 216–226 (2016).
20. Yang, L. et al. Long-lived nanosecond spin relaxation and spin coherence of electrons in monolayer MoS_2 and WS_2. *Nat. Phys.* **11**, 830–834 (2015).
21. Hsu, W.-T. et al. Optically initialized robust valley-polarized holes in monolayer WSe_2. *Nat. Commun.* **6**, 8963 (2015).

22. Dey, P. et al. Gate-controlled spin–valley locking of resident carriers in WSe_2 monolayers. *Phys. Rev. Lett.* **119**, 137401 (2017).
23. Branny, A., Kumar, S., Proux, R. & Gerardot, B. D. Deterministic strain-induced arrays of quantum emitters in a two-dimensional semiconductor. *Nat. Commun.* **8**, 15053 (2017).
24. Palacios-Berraquero, C. et al. Large-scale quantum-emitter arrays in atomically thin semiconductors. *Nat. Commun.* **8**, 15093 (2017).
25. Horng, J. et al. Perfect absorption by an atomically thin crystal. *Phys. Rev. Appl.* **14**, 024009 (2020).
26. Scuri, G. et al. Large excitonic reflectivity of monolayer $MoSe_2$ encapsulated in hexagonal boron nitride. *Phys. Rev. Lett.* **120**, 037402 (2018).
27. Back, P., Zeytinoglu, S., Ijaz, A., Kroner, M. & Imamoğlu, A. Realization of an electrically tunable narrow-bandwidth atomically thin mirror using monolayer $MoSe_2$. *Phys. Rev. Lett.* **120**, 037401 (2018).
28. Epstein, I. et al. Near-unity light absorption in a monolayer WS_2 van der Waals heterostructure cavity. *Nano Lett.* **20**, 3545–3552 (2020).
29. Jiang, S., Li, L., Wang, Z., Mak, K. F. & Shan, J. Controlling magnetism in 2D CrI_3 by electrostatic doping. *Nat. Nanotechnol.* **13**, 549–553 (2018).
30. Frindt, R. Single crystals of MoS_2 several molecular layers thick. *J. Appl. Phys.* **37**, 1928–1929 (1966).
31. Dickinson, R. G. & Pauling, L. The crystal structure of molybdenite. *J. Am. Chem. Soc.* **45**, 1466–1471 (1923).
32. Wilson, J. A. & Yoffe, A. The transition metal dichalcogenides discussion and interpretation of the observed optical, electrical and structural properties. *Adv. Phys.* **18**, 193–335 (1969).
33. Van Baren, J. et al. Stacking-dependent interlayer phonons in 3R and 2H MoS_2. *2D Mater.* **6**, 025022 (2019).
34. Frondel, J. W. & Wickman, F. E. Molybdenite polytypes in theory and occurrence. ii. some naturally-occurring polytypes of molybdenite. *Am. Mineral.* **55**, 1857–1875 (1970).
35. Xiao, D., Liu, G.-B., Feng, W., Xu, X. & Yao, W. Coupled spin and valley physics in monolayers of MoS_2 and other group-VI dichalcogenides. *Phys. Rev. Lett.* **108**, 196802 (2012).
36. Yu, H., Liu, G.-B., Tang, J., Xu, X. & Yao, W. Moirē excitons: from programmable quantum emitter arrays to spin–orbit-coupled artificial lattices. *Sci. Adv.* **3**, e1701696 (2017).
37. Dyakonov, M. I. *Spin Physics in Semiconductors*, Vol. 1 (Springer, 2017).
38. Mak, K. F., Lee, C., Hone, J., Shan, J. & Heinz, T. F. Atomically thin MoS_2: a new direct-gap semiconductor. *Phys. Rev. Lett.* **105**, 136805 (2010).
39. Splendiani, A. et al. Emerging photoluminescence in monolayer MoS_2. *Nano Lett.* **10**, 1271–1275 (2010).
40. Tonndorf, P. et al. Photoluminescence emission and Raman response of monolayer MoS_2, $MoSe_2$, and WSe_2. *Opt. Express* **21**, 4908–4916 (2013).
41. Moody, G. et al. Intrinsic homogeneous linewidth and broadening mechanisms of excitons in monolayer transition metal dichalcogenides. *Nat. Commun.* **6**, 8315 (2015).
42. Wang, G. et al. Giant enhancement of the optical second-harmonic emission of WSe_2 monolayers by laser excitation at exciton resonances. *Phys. Rev. Lett.* **114**, 097403 (2015).
43. Kormányos, A. et al. k·p theory for two-dimensional transition metal dichalcogenide semiconductors. *2D Mater.* **2**, 022001 (2015).
44. He, K. et al. Tightly bound excitons in monolayer WSe_2. *Phys. Rev. Lett.* **113**, 026803 (2014).
45. Chernikov, A. et al. Exciton binding energy and nonhydrogenic Rydberg series in monolayer WS_2. *Phys. Rev. Lett.* **113**, 076802 (2014).
46. Ugeda, M. M. et al. Giant bandgap renormalization and excitonic effects in a monolayer transition metal dichalcogenide semiconductor. *Nat. Mater.* **13**, 1091–1095 (2014).
47. Wang, G. et al. Colloquium: Excitons in atomically thin transition metal dichalcogenides. *Rev. Mod. Phys.* **90**, 021001 (2018).
48. Ramasubramaniam, A. Large excitonic effects in monolayers of molybdenum and tungsten dichalcogenides. *Phys. Rev. B* **86**, 115409 (2012).
49. Song, Y. & Dery, H. Transport theory of monolayer transition-metal dichalcogenides through symmetry. *Phys. Rev. Lett.* **111**, 026601 (2013).
50. Rytova, N. S. Screened potential of a point charge in a thin film. Preprint at https://arxiv.org/abs/1806.00976 (2018).
51. Keldysh, L. V. Coulomb interaction in thin semiconductor and semimetal films. *Sov. J. Exp. Theor. Phys. Lett.* **29**, 658 (1979).
52. Raja, A. et al. Coulomb engineering of the bandgap and excitons in two-dimensional materials. *Nat. Commun.* **8**, 15251 (2017).
53. Waldecker, L. et al. Rigid band shifts in two-dimensional semiconductors through external dielectric screening. *Phys. Rev. Lett.* **123**, 206403 (2019).
54. Rhodes, D., Chae, S. H., Ribeiro-Palau, R. & Hone, J. Disorder in van der Waals heterostructures of 2D materials. *Nat. Mater.* **18**, 541 (2019).
55. Cadiz, F. et al. Excitonic linewidth approaching the homogeneous limit in MoS_2-based van der Waals heterostructures. *Phys. Rev. X* **7**, 021026 (2017).
56. Zhou, Y. et al. Probing dark excitons in atomically thin semiconductors via near-field coupling to surface plasmon polaritons. *Nat. Nanotechnol.* **12**, 856–860 (2017).
57. Brotons-Gisbert, M. et al. Out-of-plane orientation of luminescent excitons in two-dimensional indium selenide. *Nat. Commun.* **10**, 3913 (2019).
58. Wang, G. et al. In-plane propagation of light in transition metal dichalcogenide monolayers: optical selection rules. *Phys. Rev. Lett.* **119**, 047401 (2017).
59. Robert, C. et al. Fine structure and lifetime of dark excitons in transition metal dichalcogenide monolayers. *Phys. Rev. B* **96**, 155423 (2017).
60. Robert, C. et al. Measurement of the spin-forbidden dark excitons in MoS_2 and $MoSe_2$ monolayers. *Nat. Commun.* **11**, 4037 (2020).
61. Pöllmann, C. et al. Resonant internal quantum transitions and femtosecond radiative decay of excitons in monolayer WSe_2. *Nat. Mater.* **14**, 889–893 (2015).
62. Schmidt, P. et al. Nano-imaging of intersubband transitions in van der Waals quantum wells. *Nat. Nanotechnol.* **13**, 1035–1041 (2018).
63. Liu, Y., Stradins, P. & Wei, S.-H. Van der Waals metal–semiconductor junction: weak Fermi level pinning enables effective tuning of Schottky barrier. *Sci. Adv.* **2**, e1600069 (2016).
64. Kang, J., Tongay, S., Zhou, J., Li, J. & Wu, J. Band offsets and heterostructures of two-dimensional semiconductors. *Appl. Phys. Lett.* **102**, 012111 (2013).
65. Rivera, P. et al. Observation of long-lived interlayer excitons in monolayer $MoSe_2$–WSe_2 heterostructures. *Nat. Commun.* **6**, 6242 (2015).
66. van Der Zande, A. M. et al. Tailoring the electronic structure in bilayer molybdenum disulfide via interlayer twist. *Nano Lett.* **14**, 3869–3875 (2014).
67. Weston, A. et al. Atomic reconstruction in twisted bilayers of transition metal dichalcogenides. *Nat. Nanotechnol.* **15**, 592–597 (2020).
68. Sung, J. et al. Broken mirror symmetry in excitonic response of reconstructed domains in twisted $MoSe_2$/$MoSe_2$ bilayers. *Nat. Nanotechnol.* **15**, 750–754 (2020).
69. Regan, E. C. et al. Mott and generalized Wigner crystal states in WSe_2/WS_2 moirē superlattices. *Nature* **579**, 359–363 (2020).
70. Wang, Z. et al. Evidence of high-temperature exciton condensation in two-dimensional atomic double layers. *Nature* **574**, 76–80 (2019).
71. Dau, M. T. et al. Beyond van der Waals interaction: the case of $MoSe_2$ epitaxially grown on few-layer graphene. *ACS Nano* **12**, 2319–2331 (2018).
72. Pacuski, W. Narrow excitonic lines and large-scale homogeneity of transition metal dichalcogenide monolayer grown by MBE on hBN. *Nano Lett.* **20**, 3058–3066 (2020).
73. Amani, M. et al. Near-unity photoluminescence quantum yield in MoS_2. *Science* **350**, 1065–1068 (2015).
74. Lee, Y.-H. et al. Synthesis of large-area MoS_2 atomic layers with chemical vapor deposition. *Adv. Mater.* **24**, 2320–2325 (2012).
75. Kobayashi, Y. et al. Growth and optical properties of high-quality monolayer WS_2 on graphite. *ACS Nano* **9**, 4056–4063 (2015).
76. Rhyee, J.-S. et al. High-mobility transistors based on large-area and highly crystalline CVD-grown $MoSe_2$ films on insulating substrates. *Adv. Mater.* **28**, 2316–2321 (2016).
77. George, A. et al. Controlled growth of transition metal dichalcogenide monolayers using Knudsen-type effusion cells for the precursors. *J. Phys. Mater.* **2**, 016001 (2019).
78. Sahoo, P. K., Memaran, S., Xin, Y., Balicas, L. & Gutiērrez, H. R. One-pot growth of two-dimensional lateral heterostructures via sequential edge-epitaxy. *Nature* **553**, 63–67 (2018).
79. Li, J. et al. General synthesis of two-dimensional van der Waals heterostructure arrays. *Nature* **579**, 368–374 (2020).
80. Jia, H. et al. Large-scale arrays of single-and few-layer MoS_2 nanomechanical resonators. *Nanoscale* **8**, 10677–10685 (2016).
81. Paradisanos, I. et al. Controlling interlayer excitons in MoS_2 layers grown by chemical vapor deposition. *Nat. Commun.* **11**, 2391 (2020).
82. Li, M.-Y. et al. Epitaxial growth of a monolayer WSe_2–MoS_2 lateral pn junction with an atomically sharp interface. *Science* **349**, 524–528 (2015).
83. Hsu, W.-T. et al. Evidence of indirect gap in monolayer WSe_2. *Nat. Commun.* **8**, 929 (2017).
84. Hsu, W.-T. et al. Negative circular polarization emissions from WSe_2/$MoSe_2$ commensurate heterobilayers. *Nat. Commun.* **9**, 1356 (2018).
85. Hsu, W.-T. et al. Tailoring excitonic states of van der Waals bilayers through stacking configuration, band alignment, and valley spin. *Sci. Adv.* **5**, eaax7407 (2019).
86. Raja, A. et al. Dielectric disorder in two-dimensional materials. *Nat. Nanotechnol.* **14**, 832–837 (2019).
87. Lien, D.-H. et al. Engineering light outcoupling in 2D materials. *Nano Lett.* **15**, 1356–1361 (2015).
88. Robert, C. et al. Optical spectroscopy of excited exciton states MoS_2 monolayers in van der Waals heterostructures. *Phys. Rev. Mater.* **2**, 011001 (2018).
89. Fang, H. et al. Control of the exciton radiative lifetime in van der Waals heterostructures. *Phys. Rev. Lett.* **123**, 067401 (2019).
90. Castellanos-Gomez, A. et al. Deterministic transfer of two-dimensional materials by all-dry viscoelastic stamping. *2D Mater.* **1**, 011002 (2014).
91. Purdie, D. et al. Cleaning interfaces in layered materials heterostructures. *Nat. Commun.* **9**, 5387 (2018).
92. Wang, Z., Zhao, L., Mak, K. F. & Shan, J. Probing the spin-polarized electronic band structure in monolayer transition metal dichalcogenides by optical spectroscopy. *Nano Lett.* **17**, 740–746 (2017).
93. Zhou, Y. et al. Controlling excitons in an atomically thin membrane with a mirror. *Phys. Rev. Lett.* **124**, 027401 (2020).
94. Courtade, E. et al. Charged excitons in monolayer WSe_2: experiment and theory. *Phys. Rev. B* **96**, 085302 (2017).
95. Bermudez, V. M. & McClure, D. S. Spectroscopic studies of the two-dimensional magnetic insulators chromium trichloride and chromium tribromide-I. *J. Phys. Chem. Solids* **40**, 129–147 (1979).
96. Molina-Sānchez, A., Catarina, G., Sangalli, D. & Fernāndez-Rossier, J. Magneto-optical response of chromium trihalide monolayers: chemical trends. *J. Mater. Chem. C* **8**, 8856–8863 (2020).
97. Karni, O. et al. Infrared interlayer exciton emission in MoS_2/WSe_2 heterostructures. *Phys. Rev. Lett.* **123**, 247402 (2019).
98. Ling, X., Wang, H., Huang, S., Xia, F. & Dresselhaus, M. S. The renaissance of black phosphorus. *Proc. Natl Acad. Sci. USA* **112**, 4523–4530 (2015).
99. Ansari, L. et al. Quantum confinement-induced semimetal-to-semiconductor evolution in large-area ultra-thin $PtSe_2$ films grown at 400 °C. *npj 2D Mater. Appl.* **3**, 33 (2019).
100. Cassabois, G., Valvin, P. & Gil, B. Hexagonal boron nitride is an indirect bandgap semiconductor. *Nat. Photonics* **10**, 262–266 (2016).
101. Kharche, N. & Nayak, S. K. Quasiparticle band gap engineering of graphene and graphone on hexagonal boron nitride substrate. *Nano Lett.* **11**, 5274–5278 (2011).
102. Ramasubramaniam, A., Naveh, D. & Towe, E. Tunable band gaps in bilayer graphene–BN heterostructures. *Nano Lett.* **11**, 1070–1075 (2011).
103. Spence, D. E., Kean, P. N. & Sibbett, W. 60-fsec pulse generation from a self-mode-locked Ti: sapphire laser. *Opt. Lett.* **16**, 42–44 (1991).
104. Alfano, R. R. *The Supercontinuum Laser Source: The Ultimate White Light* (Springer, 2016).
105. Arora, A. et al. Interlayer excitons in a bulk van der Waals semiconductor. *Nat. Commun.* **8**, 639 (2017).
106. Leisgang, N. et al. Giant Stark splitting of an exciton in bilayer MoS_2. *Nat. Nanotechnol.* **15**, 901–907 (2020).
107. Zhang, X.-X. et al. Magnetic brightening and control of dark excitons in monolayer WSe_2. *Nat. Nanotechnol.* **12**, 883–888 (2017).
108. Wang, G. et al. Control of exciton valley coherence in transition metal dichalcogenide monolayers. *Phys. Rev. Lett.* **117**, 187401 (2016).

109. Goryca, M. et al. Revealing exciton masses and dielectric properties of monolayer semiconductors with high magnetic fields. *Nat. Commun.* **10**, 4172 (2019).
110. Klingshirn, C. F. *Semiconductor Optics* (Springer, 2012).
111. Li, Y. et al. Measurement of the optical dielectric function of monolayer transition-metal dichalcogenides: MoS_2, $MoSe_2$, WS_2, and WSe_2. *Phys. Rev. B* **90**, 205422 (2014).
112. Ho, C., Huang, Y., Tiong, K. & Liao, P. Absorption-edge anisotropy in ReS_2 and $ReSe_2$ layered semiconductors. *Phys. Rev. B* **58**, 16130 (1998).
113. Zhang, E. et al. Tunable ambipolar polarization-sensitive photodetectors based on high-anisotropy $ReSe_2$ nanosheets. *ACS Nano* **10**, 8067–8077 (2016).
114. Horng, J. et al. Observation of interlayer excitons in $MoSe_2$ single crystals. *Phys. Rev. B* **97**, 241404 (2018).
115. Arora, A. et al. Valley-contrasting optics of interlayer excitons in Mo- and W-based bulk transition metal dichalcogenides. *Nanoscale* **10**, 15571–15577 (2018).
116. Gerber, I. C. et al. Interlayer excitons in bilayer MoS_2 with strong oscillator strength up to room temperature. *Phys. Rev. B* **99**, 035443 (2019).
117. Slobodeniuk, A. et al. Fine structure of K-excitons in multilayers of transition metal dichalcogenides. *2D Mater.* **6**, 025026 (2019).
118. Lorchat, E. et al. Dipolar and magnetic properties of strongly absorbing hybrid interlayer excitons in pristine bilayer MoS_2. Preprint at https://arxiv.org/abs/2004.12753 (2020).
119. Pelant, I. & Valenta, J. *Luminescence Spectroscopy of Semiconductors* (Oxford Univ. Press, 2012).
120. Haunschild, J. et al. Quality control of as-cut multicrystalline silicon wafers using photoluminescence imaging for solar cell production. *Solar Energy Mater. Solar Cells* **94**, 2007–2012 (2010).
121. Balocchi, A., Amand, T. & Marie, X. in *Semiconductor Research* (eds Patane, A. & Balkan, N.) 223–258 (Springer, 2012).
122. Jakubczyk, T. et al. Radiatively limited dephasing and exciton dynamics in $MoSe_2$ monolayers revealed with four-wave mixing microscopy. *Nano Lett.* **16**, 5333–5339 (2016).
123. Hao, K. et al. Coherent and incoherent coupling dynamics between neutral and charged excitons in monolayer $MoSe_2$. *Nano Lett.* **16**, 5109–5113 (2016).
124. Robert, C. et al. Fine structure and lifetime of dark excitons in transition metal dichalcogenide monolayers. *Phys. Rev. B* **96**, 155423 (2017).
125. Shree, S. et al. Observation of exciton-phonon coupling in $MoSe_2$ monolayers. *Phys. Rev. B* **98**, 035302 (2018).
126. Nagler, P. et al. Zeeman splitting and inverted polarization of biexciton emission in monolayer WS_2. *Phys. Rev. Lett.* **121**, 057402 (2018).
127. Sun, D. et al. Observation of rapid exciton–exciton annihilation in monolayer molybdenum disulfide. *Nano Lett.* **14**, 5625–5629 (2014).
128. Barbone, M. et al. Charge-tuneable biexciton complexes in monolayer WSe_2. *Nat. Commun.* **9**, 3721 (2018).
129. Paradisanos, I. et al. Room temperature observation of biexcitons in exfoliated WS_2 monolayers. *Appl. Phys. Lett.* **110**, 193102 (2017).
130. Sigl, L. et al. Condensation signatures of photogenerated interlayer excitons in a van der Waals heterostack. Preprint at https://arxiv.org/abs/2001.07567 (2020).
131. Taniguchi, T. & Watanabe, K. Synthesis of high-purity boron nitride single crystals under high pressure by using Ba-BN solvent. *J. Cryst. Growth* **303**, 525–529 (2007).
132. Zhu, C. et al. Strain tuning of optical emission energy and polarization in monolayer and bilayer MoS_2. *Phys. Rev. B* **88**, 121301 (2013).
133. Berger, S. et al. Optical properties of carbon nanotubes in a composite material: the role of dielectric screening and thermal expansion. *J. Appl. Phys.* **105**, 094323 (2009).
134. Hirana, Y., Tanaka, Y., Niidome, Y. & Nakashima, N. Strong micro-dielectric environment effect on the band gaps of (n,m) single-walled carbon nanotubes. *J. Am. Chem. Soc.* **132**, 13072–13077 (2010).
135. Ai, N., Walden-Newman, W., Song, Q., Kalliakos, S. & Strauf, S. Suppression of blinking and enhanced exciton emission from individual carbon nanotubes. *ACS Nano* **5**, 2664–2670 (2011).
136. Noe, J. C. et al. Environmental electrometry with luminescent carbon nanotubes. *Nano Lett.* **18**, 4136–4140 (2018).
137. Raynaud, C. et al. Superlocalization of excitons in carbon nanotubes at cryogenic temperature. *Nano Lett.* **19**, 7210–7216 (2019).
138. Blancon, J.-C. et al. Scaling law for excitons in 2D perovskite quantum wells. *Nat. Commun.* **9**, 1–10 (2018).
139. Zhang, H. et al. Interference effect on optical signals of monolayer MoS_2. *Appl. Phys. Lett.* **107**, 101904 (2015).
140. Roddaro, S., Pingue, P., Piazza, V., Pellegrini, V. & Beltram, F. The optical visibility of graphene: interference colors of ultrathin graphite on SiO_2. *Nano Lett.* **7**, 2707–2710 (2007).
141. Lagarde, D. et al. Carrier and polarization dynamics in monolayer MoS_2. *Phys. Rev. Lett.* **112**, 047401 (2014).
142. Robert, C. et al. Exciton radiative lifetime in transition metal dichalcogenide monolayers. *Phys. Rev. B* **93**, 205423 (2016).
143. Bandurin, D. A. et al. High electron mobility, quantum Hall effect and anomalous optical response in atomically thin InSe. *Nat. Nanotechnol.* **12**, 223 (2017).
144. Liu, E. et al. Multipath optical recombination of intervalley dark excitons and trions in monolayer WSe_2. *Phys. Rev. Lett.* **124**, 196802 (2020).
145. Luo, Y. et al. Exciton dipole orientation of strain-induced quantum emitters in WSe_2. *Nano Lett.* **20**, 5119–5126 (2020).
146. Lu, Z. et al. Magnetic field mixing and splitting of bright and dark excitons in monolayer $MoSe_2$. *2D Mater.* **7**, 015017 (2019).
147. Rivera, P. et al. Interlayer valley excitons in heterobilayers of transition metal dichalcogenides. *Nat. Nanotechnol.* **13**, 1004–1015 (2018).
148. Jauregui, L. A. et al. Electrical control of interlayer exciton dynamics in atomically thin heterostructures. *Science* **366**, 870–875 (2019).
149. Mupparapu, R., Bucher, T. & Staude, I. Integration of two-dimensional transition metal dichalcogenides with Mie-resonant dielectric nanostructures. *Adv. Phys. X* **5**, 1734083 (2020).
150. Vasista, A. B., Sharma, D. K. & Kumar, G. P. Fourier plane optical microscopy and spectroscopy. *Digital Encyclopedia of Applied Physics* https://doi.org/10.1002/3527600434.eap817 (2003).
151. Vasista, A. B. et al. Differential wavevector distribution of surface-enhanced Raman scattering and fluorescence in a film-coupled plasmonic nanowire cavity. *Nano Lett.* **18**, 650–655 (2018).
152. Gu, J., Chakraborty, B., Khatoniar, M. & Menon, V. M. A room-temperature polariton light-emitting diode based on monolayer WS_2. *Nat. Nanotechnol.* **14**, 1024–1028 (2019).
153. Wagner, R., Heerklotz, L., Kortenbruck, N. & Cichos, F. Back focal plane imaging spectroscopy of photonic crystals. *Appl. Phys. Lett.* **101**, 081904 (2012).
154. Graf, A., Tropf, L., Zakharko, Y., Zaumseil, J. & Gather, M. C. Near-infrared exciton-polaritons in strongly coupled single-walled carbon nanotube microcavities. *Nat. Commun.* **7**, 13078 (2016).
155. Yoshikawa, K., Matsuda, K. & Kanemitsu, Y. Exciton transport in suspended single carbon nanotubes studied by photoluminescence imaging spectroscopy. *J. Phys. Chem. C* **114**, 4353–4356 (2010).
156. Cadiz, F. et al. Exciton diffusion in WSe_2 monolayers embedded in a van der Waals heterostructure. *Appl. Phys. Lett.* **112**, 152106 (2018).
157. Kulig, M. et al. Exciton diffusion and halo effects in monolayer semiconductors. *Phys. Rev. Lett.* **120**, 207401 (2018).
158. Rivera, P. et al. Valley-polarized exciton dynamics in a 2D semiconductor heterostructure. *Science* **351**, 688–691 (2016).
159. Unuchek, D. et al. Valley-polarized exciton currents in a van der Waals heterostructure. *Nat. Nanotechnol.* **14**, 1104–1109 (2019).
160. Hong, X. et al. Ultrafast charge transfer in atomically thin MoS_2/WS_2 heterostructures. *Nat. nanotechnol.* **9**, 682–686 (2014).
161. Ciarrocchi, A. et al. Polarization switching and electrical control of interlayer excitons in two-dimensional van der Waals heterostructures. *Nat. Photonics* **13**, 131–136 (2019).
162. Hill, H. M. et al. Observation of excitonic Rydberg states in monolayer MoS_2 and WS_2 by photoluminescence excitation spectroscopy. *Nano Lett.* **15**, 2992–2997 (2015).
163. Srivastava, A. & Imamoğlu, A. Signatures of Bloch-band geometry on excitons: nonhydrogenic spectra in transition-metal dichalcogenides. *Phys. Rev. Lett.* **115**, 166802 (2015).
164. Glazov, M. et al. Intrinsic exciton-state mixing and nonlinear optical properties in transition metal dichalcogenide monolayers. *Phys. Rev. B* **95**, 035311 (2017).
165. Berghäuser, G., Knorr, A. & Malic, E. Optical fingerprint of dark 2*p*-states in transition metal dichalcogenides. *2D Mater.* **4**, 015029 (2016).
166. Wang, G. et al. Exciton states in monolayer $MoSe_2$: impact on interband transitions. *2D Mater.* **2**, 045005 (2015).
167. Chow, C. M. et al. Phonon-assisted oscillatory exciton dynamics in monolayer $MoSe_2$. *npj 2D Mater. Appl.* **1**, 33 (2017).
168. Soubelet, P. et al. Resonance effects in the Raman scattering of monolayer and few-layer $MoSe_2$. *Phys. Rev. B* **93**, 155407 (2016).
169. Kioseoglou, G. et al. Valley polarization and intervalley scattering in monolayer MoS_2. *Appl. Phys. Lett.* **101**, 221907 (2012).
170. Tornatzky, H., Kaulitz, A.-M. & Maultzsch, J. Resonance profiles of valley polarization in single-layer MoS_2 and $MoSe_2$. *Phys. Rev. Lett.* **121**, 167401 (2018).
171. Dufferwiel, S. et al. Valley-addressable polaritons in atomically thin semiconductors. *Nat. Photonics* **11**, 497–501 (2017).
172. Dufferwiel, S. et al. Valley coherent exciton-polaritons in a monolayer semiconductor. *Nat. Commun.* **9**, 4797 (2018).
173. Paradisanos, I. et al. Prominent room temperature valley polarization in WS_2/graphene heterostructures grown by chemical vapor deposition. *Appl. Phys. Lett.* **116**, 203102 (2020).
174. Rosenberger, M. R. et al. Twist angle-dependent atomic reconstruction and moiré patterns in transition metal dichalcogenide heterostructures. *ACS Nano* **14**, 4550–4558 (2020).
175. Yu, H., Liu, G.-B. & Yao, W. Brightened spin-triplet interlayer excitons and optical selection rules in van der Waals heterobilayers. *2D Mater.* **5**, 035021 (2018).
176. Molas, M. et al. Probing and manipulating valley coherence of dark excitons in monolayer WSe_2. *Phys. Rev. Lett.* **123**, 096803 (2019).
177. Srivastava, A. et al. Valley Zeeman effect in elementary optical excitations of monolayer WSe_2. *Nat. Phys.* **11**, 141–147 (2015).
178. Nagler, P. et al. Giant magnetic splitting inducing near-unity valley polarization in van der Waals heterostructures. *Nat. Commun.* **8**, 1551 (2017).
179. Back, P. Giant magnetic splitting inducing near-unity valley polarization in van der Waals heterostructures. *Phys. Rev. Lett.* **118**, 237404 (2017).
180. Carvalho, B. R., Malard, L. M., Alves, J. M., Fantini, C. & Pimenta, M. A. Symmetry-dependent exciton-phonon coupling in 2D and bulk MoS_2 observed by resonance Raman scattering. *Phys. Rev. Lett.* **114**, 136403 (2015).
181. Scheuschner, N., Gillen, R., Staiger, M. & Maultzsch, J. Interlayer resonant Raman modes in few-layer MoS_2. *Phys. Rev. B* **91**, 235409 (2015).
182. Oliver, S. M. et al. The structural phases and vibrational properties of $Mo_{1-x}W_xTe_2$ alloys. *2D Mater.* **4**, 045008 (2017).
183. Wolverson, D., Crampin, S., Kazemi, A. S., Ilie, A. & Bending, S. J. Raman spectra of monolayer, few-layer, and bulk $ReSe_2$: an anisotropic layered semiconductor. *ACS Nano* **8**, 11154–11164 (2014).
184. Chakraborty, B. et al. Symmetry-dependent phonon renormalization in monolayer MoS_2 transistor. *Phys. Rev. B* **85**, 161403 (2012).
185. Bertolazzi, S. et al. Engineering chemically active defects in monolayer MoS_2 transistors via ion-beam irradiation and their healing via vapor deposition of alkanethiols. *Adv. Mater.* **29**, 1606760 (2017).
186. Conley, H. J. et al. Bandgap engineering of strained monolayer and bilayer MoS_2. *Nano Lett.* **13**, 3626–3630 (2013).
187. Mignuzzi, S. et al. Effect of disorder on Raman scattering of single-layer MoS_2. *Phys. Rev. B* **91**, 195411 (2015).
188. Buscema, M., Steele, G. A., van der Zant, H. S. & Castellanos-Gomez, A. The effect of the substrate on the Raman and photoluminescence emission of single-layer MoS_2. *Nano Res.* **7**, 561–571 (2014).
189. Lee, C. et al. Anomalous lattice vibrations of single- and few-layer MoS_2. *ACS Nano* **4**, 2695–2700 (2010).

190. Zhang, X. et al. Raman spectroscopy of shear and layer breathing modes in multilayer MoS_2. *Phys. Rev. B* **87**, 115413 (2013).
191. Debnath, R. et al. Evolution of high-frequency Raman modes and their doping dependence in twisted bilayer MoS_2. *Nanoscale* **12**, 17272–17280 (2020).
192. Hsu, W.-T. et al. Second harmonic generation from artificially stacked transition metal dichalcogenide twisted bilayers. *ACS Nano* **8**, 2951–2958 (2014).
193. Shinde, S. M. et al. Stacking-controllable interlayer coupling and symmetric configuration of multilayered MoS_2. *NPG Asia Mater.* **10**, e468 (2018).
194. Psilodimitrakopoulos, S. et al. Twist angle mapping in layered WS_2 by polarization-resolved second harmonic generation. *Sci. Rep.* **9**, 14285–11 (2019).
195. Psilodimitrakopoulos, S. et al. Ultrahigh-resolution nonlinear optical imaging of the armchair orientation in 2D transition metal dichalcogenides. *Light Sci. Appl.* **7**, 18005 (2018).
196. Mennel, L., Paur, M. & Mueller, T. Second harmonic generation in strained transition metal dichalcogenide monolayers: MoS_2, $MoSe_2$, WS_2, and WSe_2. *APL Photonics* **4**, 034404 (2019).
197. Farenbruch, A. et al. Magneto-Stark and Zeeman effect as origin of second harmonic generation of excitons in Cu_2O. *Phys. Rev. B* **101**, 115201 (2020).
198. Seyler, K. L. et al. Electrical control of second-harmonic generation in a WSe_2 monolayer transistor. *Nat. Nanotechnol.* **10**, 407–411 (2015).
199. Kaminski, B. et al. Spin-induced optical second harmonic generation in the centrosymmetric magnetic semiconductors EuTe and EuSe. *Phys. Rev. Lett.* **103**, 057203 (2009).
200. Sun, Z. et al. Topographic and electronic contrast of the graphene moirē on Ir(111) probed by scanning tunneling microscopy and noncontact atomic force microscopy. *Phys. Rev. B* **83**, 081415 (2011).
201. de la Torre, B. et al. Atomic-scale variations of the mechanical response of 2D materials detected by noncontact atomic force microscopy. *Phys. Rev. Lett.* **116**, 245502 (2016).
202. Darlington, T. P. et al. Imaging strain-localized excitons in nanoscale bubbles of monolayer WSe_2 at room temperature. *Nat. Nanotechnol.* **15**, 854–860 (2020).
203. Cao, T. et al. Valley-selective circular dichroism of monolayer molybdenum disulphide. *Nat. Commun.* **3**, 887 (2012).
204. Mak, K. F., He, K., Shan, J. & Heinz, T. F. Control of valley polarization in monolayer MoS_2 by optical helicity. *Nat. Nanotechnol.* **7**, 494–498 (2012).
205. Sallen, G. et al. Robust optical emission polarization in MoS_2 monolayers through selective valley excitation. *Phys. Rev. B* **86**, 081301 (2012).
206. Zeng, H., Dai, J., Yao, W., Xiao, D. & Cui, X. Valley polarization in MoS_2 monolayers by optical pumping. *Nat. Nanotechnol.* **7**, 490–493 (2012).
207. Unuchek, D. *Spin–Valley Optoelectronics Based on Two-dimensional Materials*. Thesis, EPFL (2019).
208. Hecht, E. et al. *Optics* Vol. 4 (Addison Wesley, 2002).
209. Pawley, J. *Handbook of Biological Confocal Microscopy* Vol. 236 (Springer, 2006).
210. Kuhlmann, A. V. et al. A dark-field microscope for background-free detection of resonance fluorescence from single semiconductor quantum dots operating in a set-and-forget mode. *Rev. Sci. Instrum.* **84**, 073905 (2013).
211. Benelajla, M., Kammann, E., Urbaszek, B. & Karrai, K. The physical origins of extreme cross-polarization extinction in confocal microscopy. Preprint at https://arxiv.org/abs/2004.13564 (2020).

Acknowledgements
The authors acknowledge funding from ANR 2D-vdW-Spin, ANR ValleEx, ANR MagicValley, ITN 4PHOTON Marie Sklodowska Curie Grant Agreement no. 721394 and the Institut Universitaire de France. The authors thank H. Tornatzky, D. Lagarde, A. Balocchi, N. Leisgang, H. Park and M. Glazov for discussions, and Y. Zhou for providing data from Zhou et al. *Phys. Rev. Lett.* **124**, 027401 (2020).

Author contributions
All authors contributed to the discussion of content and researched data for the article. S.S., I.P. and C.R. wrote the manuscript with critical input from X.M. and B.U.

Competing interests
The authors declare no competing interests.

Publisher's note
Springer Nature remains neutral with regard to jurisdictional claims in published maps and institutional affiliations.